Preprint: Linking the core heat content to Earth's accretion history

Vincent Clesi[1,2], Renaud Deguen[3,1]

25/03/2023

[1] Univ Lyon, ENSL, UCBL, UJM, CNRS, LGL-TPE, F-69007 Lyon, France
[2] Rice University Department of Earth Science. Keith-Wiess Geological Laboratory. 6100 Main Street Houston
[3] Univ. Grenoble Alpes, Univ. Savoie Mont Blanc, CNRS, IRD, Univ. Gustave Eiffel, ISTerre, 38000 Grenoble, France

This version is a preprint of a paper entitle: '**Linking the core heat content to Earth's accretion history**' reviewed and accepted by the editorial board, in production at Geochemistry, Geophysics, Geosystems with no doi assigned at the date of deposit on the EarthArXiv repository (25th of March 2023). It contains the main text and the supplementary materials.

Linking the core heat content to Earth's accretion history

Vincent Clesi[1,2], **Renaud Deguen**[3,1]

[1]Univ Lyon, ENSL, UCBL, UJM, CNRS, LGL-TPE, F-69007 Lyon, France

[2]Rice University Department of Earth Science. Keith-Wiess Geological Laboratory. 6100 Main Street Houston

[3]Univ. Grenoble Alpes, Univ. Savoie Mont Blanc, CNRS, IRD, Univ. Gustave Eiffel, ISTerre, 38000 Grenoble, France

Corresponding author: Vincent Clesi, vincentclesi@rice.edu

Abstract

The primordial heat content of the core and its initial composition are important parameters for the thermal and magnetic evolutions of the core, as well as for the physical and chemical state of the core as it is today. In this study we use a parameterized model of differentiation in a magma ocean setting, in which the magma ocean depth evolves during accretion, to predict the composition of the primordial core. We couple this chemical model to a thermal evolution model of the accreting metal to estimate the Earth's core heat content at the end of its formation. We find that a range of differentiation scenarios, having different evolutions of the metal-silicates equilibration pressure and temperature, can result in geochemically consistent models (*i.e.* having a mantle composition similar to the BSE). All these scenarios have in common two key features: (i) the average pressure of metal-silicates equilibration is between 20 and 45 GPa (final pressure between 40 and 60% of CMB pressure); (ii) 60 to 80% of Earth's mass is accreted as reduced material with Si contents between 1.5 and 6 % wt of the core, and O contents between 1 and 2 % wt. The chemical stratification is stable in most cases, though some scenarios result in an unstable compositional stratification. Mixing an initially stratified core requires a small fraction (between 1 and 10 %) of the energy released after a giant impact. Importantly, our geochemically consistent scenarios each result in different core temperatures, the temperature at the Core Mantle Boundary (CMB) after mixing the core to an isentropic state ranging from 3925 to 4150 K. For example, scenarios in which the magma ocean remains shallow for a large part of the accretion, and then gets deeper at the end of accretion can produce chemically coherent models with cooler cores. This suggests that independent constraints on the core temperature could in principle be used as constraints for the differentiation conditions, and core composition. In particular, we find that the abundance of light elements in the core correlates positively with the temperature of the core at the end of accretion, as well as with the average pressure of equilibration during differentiation.

1 Introduction

The physical and chemical properties of the early core are important for the thermal and magnetic evolution of the core, as well as to understand the current properties of the Earth's core such as core density deficit (Dziewonski & Anderson, 1981) or tem-

perature (Hirose et al., 2013; Labrosse, 2015). The initial conditions in temperature and composition of the Earth's core are important to understand how and when the inner core started to crystallize and how it can trigger and sustain the Earth's magnetic field by itself (de Koker et al., 2012; Badro et al., 2018), or contribute to a thermally driven dynamo (Andrault et al., 2016). The presence of light elements in the core has been attested by the study of seismological data compared to pure iron equation of state (Birch, 1964) and it has an impact on the temperature profile of the Earth's core, as there is a compositional dependence of the liquidus temperature and latent heat release at the ICB (Inner Core Boundary) (Labrosse, 2015).

The nature and concentrations of the light elements in the core have been explained by metal/silicate partitioning experiments at high pressure. Those partitioning experiments are designed to model the core/mantle segregation process in a magma ocean. There is strong evidences that the core/mantle segregation process happened in a deep magma ocean. Firstly, large impactors can release enough energy to melt the primordial mantle almost completely, especially at the end of accretion (Tonks & Melosh, 1993; Canup, 2004). Secondly, the timescale of core formation from Hf/W systematics indicates a relatively rapid (between 30 and 100 Myrs) core segregation and high equilibrium efficiency (Kleine et al., 2009; Nimmo & Kleine, 2015), the latter being better explained by liquid-liquid segregation of metal and silicate (Rubie et al., 2003). Finally, the siderophile elements abundances indicates that metal and silicate equilibrated deep in the magma ocean (Drake & Righter, 2002; M. A. Bouhifd & Jephcoat, 2003), which has implications for the nature and abundance of light elements in the core. The theory of a deep magma ocean has lead to the creation of important models of Earth's core accretion and segregation based on the partitioning behavior of siderophile elements. Ni and Co partitioning behaviour put constraints on the maximum extent of the magma ocean (to a depth between 40 to 60 % of the CMB depth M. Bouhifd & Jephcoat, 2011; Siebert et al., 2012), while the partitioning of the less siderophile elements (V,Cr, Mn, Nb, Ta), for which partitioning behavior is more dependent on oxygen fugacity (Wood et al., 2008; Tuff et al., 2011; Cartier, Hammouda, Doucelance, et al., 2014) showed that the conditions of mantle/core segregation on the Earth became more oxidized (Wood et al., 2008; Fischer et al., 2015; Rubie et al., 2015). These models also provide predictions of light elements abundances accounting for the core density deficit, mostly Si and O (Tsuno et al., 2013; Fischer et al., 2015) with an important contribution from S (Boujibar et al.,

2014; Laurenz et al., 2016). Some trace elements could also contribute to the core density deficit such as C (Chi et al., 2014; Dasgupta & Grewal, 2019), H (Clesi et al., 2018; Malavergne et al., 2019) and N (Roskosz et al., 2013; Speelmanns et al., 2018).

Other elements may also have contributed to the onset of the geodynamo (such as Mg, Badro et al., 2018), or to the heat budget and thermal evolution of the early core (for instance U or K, M. A. Bouhifd et al., 2007; Faure et al., 2020). Putting constraints on the energy budget of the core is important for understanding the thermal and magnetic evolution of the core, and constraining the age of the inner core (Nimmo, 2007; Seagle et al., 2013; Labrosse, 2015).

The inner-core is much younger than the Earth's (0.5 to 1.5 Gyrs, Labrosse, 2015), and its crystallization has a significant impact on the geodynamo (Landeau et al., 2017). Estimating the initial heat content and the heat fluxes at the CMB is then important to explain the current thermal state of the core (Nimmo, 2007; Seagle et al., 2013; Labrosse, 2015; Andrault et al., 2016). The initial heat budget depend on the physical process of core formation. A core formed by diapirism tend to be cooler, as the gravitational energy released during core formation is dissipated mostly in the silicates rather than in the metal (Ke & Solomatov, 2009; Monteux et al., 2009).

On the other hand, a higher fraction of the gravitational energy would be released in the metal if it separated from the silicates through channels (Ke & Solomatov, 2009) or as an emulsion in a trail conduit (King & Olson, 2011; Fleck et al., 2018). The incorporation of heat producing element (Faure et al., 2020) into the core also has an influence on the initial heat content and its evolution through time (Seagle et al., 2013; Labrosse, 2015).

In this study, we aim at linking the chemical models that explains the core density deficit and the bulk silicate earth (BSE) composition through metal/silicate equilibrium in a magma ocean (e.g. Fischer et al., 2015) and provide at the same time an estimate of the Earth's core heat content and temperature by using a thermal model to calculate the evolution of the temperature of the metal while it sinks to form the core. We use a model of continuous accretion where we parameterize the pressure and temperature of metal/silicate equilibrium, and apply to the resulting metallic phase a thermal evolution model through the solid mantle and core growth. At the end of the calculation, we get a composition for a stratified core, a bulk composition for the mantle

and the initial heat content of the core that can be attributed to core formation, for models that are chemically coherent with the Earth chondritic composition (McDonough & Sun, 1995; McDonough, 2003).

2 Thermal evolution of the metal phase

Our model follows the deep magma ocean conceptual model, according to which the Earth is covered by a magma ocean which depth evolves with time as accretion proceeds. Each impact delivers a mass of metal δM_m, which is assumed to disperse in the magma ocean, accumulate at its base, and migrate through the solid part of the mantle as a diapir of radius R_d.

We develop here an analytical model for the thermal evolution of the metal phase increment during its descent through the solid mantle toward the growing core, taking into account compression heating, viscous dissipation heating, and heat exchange with the surrounding silicates. The mass of the Earth is a fraction f of its final mass; the final thermal state of the core will be obtained by considering the full accretion history, each metal mass increment evolving according to the model described in this section. The parameters used in the model will be described in this section, and the list of parameter is given in Table 1.

The model involves three steps which are detailed below.

2.1 Initial conditions

We do not model heat transfer between metal and silicates within the magma ocean. Instead, we assume that the metal phase equilibrates thermally with the surrounding silicates, so that the pressure and temperature of the metal when it accumulates at the base of the magma ocean are equal to the pressure $P_{\rm eq}(f)$ and temperature $T_{\rm eq}(f)$ defining the lower boundary of the magma ocean. Since Hf-W systematics and siderophiles abundance in the BSE argue for significant metal-silicates chemical equilibration (Kleine et al., 2009), it seems reasonable to assume that the metal equilibrates thermally with the silicates at the base of the magma ocean.

Symbol	Parameter or variable	Value(s) and unit
$P_{\rm eq}$	Pressure at the base of magma ocean	Pa or GPa
$T_{\rm eq}$	Temperature at the base of magma ocean	K
f	Accreted mass fraction of the Earth	[0.05;1] no units
$R_\oplus$	Radius of the Earth	6370 km- 6.370 10^6 m
$R_\oplus(f)$	Radius of the Earth at a given step of accretion	$R_\oplus \times f^{1/3}$
$R_{\rm CMB}(f)$	Radius of the core at a given step of accretion	$3470 \times f^{1/3}$ km
G	Gravitational constant	6.674×10^{-11}m^3.kg^{-1}.s^{-2}
K_d	Exchange partitioning coefficient (molar)	-
χ_i^p	Concentration of element i in phase p	- wt% or mol% (see text)
$c_{p,s}$	Specific heat of silicate	500 J.kg^{-1}.K^{-1}
$c_{p,m}$	Specific heat of metal	1000 J.kg^{-1}.K^{-1}
Pe	Peclet number	- no unit
γ	Grüneisen parameter	- (no unit)
ρ_p	Density of phase p	-kg.m^{-3}
ρ_0	Density of metal at P=0	-kg.m^{-3}
g	gravity field	- m.s^{-2}
R_d	Radius of metallic diapirs	- m
$K_{S,m}$	Isentropic bulk modulus of metal	- GPa
T_{sm}	Temperature of solid mantle	-K
ε	Fraction of dissipation energy going into the metal	- no unit
α_T	Thermal expansion coefficient of metal	1.1 10^{-5}K^{-1}
P_{center}	Final pressure at the centre of the Earth	360 GPa
$\alpha_{element}$	expansion coefficient of an element	no unit
$Q_{\rm core}$	Heat content of the core after accretion	- J
$T^{\rm is}_{\rm CMB}$	Temperature at CMB after mixing the core to an isentropic state	-K
$\delta^{BSE}\chi_i$	Relative variation of χ_i to the BSE	- %
μ_s	Viscosity of solid mantle	10^{18} Pa.s
D_s	Thermal diffusion coefficient of mantle	10^{-6} m^2.s^{-1}

Table 1. List of the symbols used in this study. When no value is given in the third column, the values are calculated in the model.

2.2 Migration to the core

We now turn to describe the evolution of the metal phase while it migrates from the bottom of the magma ocean to the core, its pressure evolving in this process from $P_{\rm eq}(f)$ to the core-mantle boundary pressure $P_{\rm CMB}(f)$. Irrespectively of the mode of migration, the evolution of the temperature T of the metal is given by an equation of the form

$$C_{p,m}\frac{dT}{dt} = C_{p,m}\frac{\gamma\, T}{K_{S,m}}\frac{dP}{dt} - Q_{m\rightarrow s} + \Phi_m, \tag{1}$$

where $C_{p,m}$ is the total heat capacity of the metal mass (*i.e.* $\delta M_m c_{p,m}$, where $c_{p,m}$ is the metal specific heat capacity), γ is the Gruneisen parameter, $K_{S,m}$ is the isentropic bulk modulus, $Q_{m\rightarrow s}$ is the heat flux from the metal to the surrounding silicates, and Φ_m is dissipative (*i.e.* viscous) heating in the metal phase. The first term on the right-hand side corresponds to compression heating.

Instead of solving Equation 1 to obtain T as a function of time, we transform it into an equation for T as a function of P, using the chain rule of derivation

$$\frac{d(\cdot)}{dt} = \frac{dz}{dt}\frac{dP}{dz}\frac{d(\cdot)}{dP} = v_d\rho_s g\frac{d(\cdot)}{dP}, \tag{2}$$

where v_d is the downward velocity of the metal phase. This allows to transform Equation 1 into the more convenient form

$$\frac{dT}{dP} = \frac{\gamma\, T}{K_{S,m}} - \frac{Q_{m\rightarrow s}}{C_{p,m}v\rho_s g} + \frac{\Phi_m}{C_{p,m}v_d\rho_s g}, \tag{3}$$

which will be integrated from $P = P_{\rm eq}(f)$ to the CMB pressure $P_{\rm CMB}(f)$.

2.2.1 Compression heating

If metal to silicates heat transfer and dissipative heating are both neglected ($Q_{m\rightarrow s} = 0$ and $\Phi_m = 0$), then Equation 3 reduces to

$$\frac{dT}{dP} = \frac{\gamma\, T}{K_{S,m}} \tag{4}$$

and the temperature of the metal phase simply follows an isentrope.

2.2.2 Dissipative heating

If the metal migrates with negligible inertia (*i.e.* if the flow around the diapir is a creeping flow, as expected given the high viscosity of the surrounding silicates), then

the total rate of energy dissipation is equal to the rate of change of gravitational energy E_p, which is approximately given by the product of mass anomaly $\frac{4\pi}{3}R_d^3\Delta\rho$, gravity g, and rate of change of the height of the diapir center of mass (*i.e.* its velocity):

$$\frac{dE_p}{dt} \simeq \frac{4\pi}{3}R_d^3\Delta\rho\, g\, v_d. \tag{5}$$

with $\Delta\rho = \rho_m - \rho_s$ the difference between the density of metal and the surrounding silicate and R_d the radius of the metallic diapir. This is an approximate expression because we do not take into account the modification of the gravity field associated with the displacement of the diapir mass. Of this, only a fraction is dissipated into heat in the metal, the remaining being released in the silicates or converted into strain energy. We denote by Φ_m and Φ_s the rate of dissipation in the metal and surrounding silicates, respectively, the rate of dissipative heating within the diapir being some fraction ϵ of the total rate of change of the potential energy, *i.e.* $\Phi_m = \epsilon\frac{dE_p}{dt}$. As shown below, the ratio Φ_m/Φ_s, and therefore ϵ, are likely small (Monteux et al., 2009; Samuel et al., 2010).

In the silicates surrounding the diapir, the velocity field v varies smoothly over a lengthscale $\sim R_d$ with an amplitude v_d (e.g. Batchelor, 1967, chapter 4.9). The dissipation rate per unit of volume, $\mu_s(\nabla v + \nabla v^T) : \nabla v$, is then be $\sim \mu_s v_d^2/R_d^2$, where μ_s is the dynamic viscosity of the silicates. The total dissipation rate in the silicates is

$$\Phi_s \sim R_d^3\mu_s v_d^2/R^2 \sim \mu_s R_d v_d^2. \tag{6}$$

In fact in the $\Phi_m \to 0$ limit in which the diapir velocity is given by the Stokes velocity for an inviscid sphere ($\mu_m = 0$ Pa.s)

$$v_d = \frac{\Delta\rho g R_d^2}{3\mu_s}, \tag{7}$$

the rate of dissipation is given by $4\pi\mu_s R_d v_d^2$, an expression which can be obtained either by substituting $\Delta\rho g R_d^2$ with $3\mu_s v_d$ (from Equation 7) in Equation 5, or by multiplying the Stokes drag force ($4\pi\mu_s R_d v_d$) with the velocity v_d. The diapir velocity would be somewhat smaller than predicted by Equation 7 if the viscosity of the metal is taken into account, but the effect is expected to be small because the velocity of the diapir is always controlled by the rate at which the surrounding silicates can deform (no more than a factor of 2/3 in the unlikely limit of a diapir with $\eta_m \gg \eta_s$, according to the Stokes-Hadamard solution for a viscous sphere falling into a fluid with different viscosity (Batchelor, 1967, chapter 4.9). In the following, we will use Equation 7 when estimating the diapir velocity.

Having obtained an order-of-magnitude expression for Φ_s, we now turn to estimating the dissipation Φ_m in the diapir, assuming the flow within the diapir to be either laminar or turbulent.

If the flow within the diapir is laminar, then it will consist in a large scale axisymmetric vortex in which the velocity v varies over a length scale $\sim R_d$, with an amplitude v_d. Denoting by μ_m the viscosity of the metal, the dissipation rate per unit of volume is then $\sim \mu_m v_d^2/R_d^2$, and the total dissipation rate is $\sim R_d^3 \mu_m v_d^2/R^2 \sim R_d \mu_m v_d^2$. Comparing dissipation in the silicates (Equation 6) and metal, we have

$$\frac{\Phi_m}{\Phi_s} \sim \frac{\mu_m}{\mu_s}, \tag{8}$$

which is very small: taking for example $\mu_s = 10^{15}$ Pa.s for the silicates (a fairly low estimate taking into account the possibility of partial melting) and $\mu_m = 10^{-2}$ Pa.s (Kono et al., 2015) gives $\Phi_m/\Phi_s = 10^{-17}$.

If instead the flow withing the diapir is turbulent, then the rate of dissipation would scale as the rate of kinetic energy input, which scales as the kinetic energy of the diapir, $\frac{1}{2}\delta M_m \, v_d^2 \sim \rho_m R_d^3 v_d^2$, divided by the overturn time R_d/v_d (Tennekes & Lumley, 1972). This gives

$$\Phi_m \sim \rho_m R_d^2 v_d^3 \tag{9}$$

and, taking again $\Phi_s \sim \mu_s R_d v_d^2$ from Equation 6, we obtain

$$\frac{\Phi_m}{\Phi_s} \sim \frac{\rho_m}{\rho_s} Re_s, \tag{10}$$

where

$$Re_s = \rho_s \frac{R_d v_d}{\mu_s} \tag{11}$$

is the Reynolds number of the diapir, defined with the viscosity of the silicates. The value of Re_s depends on the size of the diapir and viscosity of the mantle, but is likely very small. Taking for example $\mu_s = 10^{18}$ Pa.s and $R_d = 100$ km gives $v_d = 7{\times}10^{-5}\mathrm{m.s}^{-1} =$ 20 cm/hour, $Re_s = 3 \times 10^{-14}$ and $\Phi_m/\Phi_s \simeq 6 \times 10^{-14}$. Maximizing the value of Re_s by taking $\mu_s = 10^{16}$ Pa.s and $R_d = 1000$ km gives $Re_s \simeq 3 \times 10^{-7}$ and $\Phi_m/\Phi_s \simeq 6 \times 10^{-7}$, which is still small, albeit not as much as in the laminar case. This therefore suggests that dissipative heating would in general have a negligible effect of the thermal evolution of the diapirs.

180 ### 2.2.3 Metal to silicates heat transfer

The discussion in section 2.2.2 suggests that dissipation happens almost exclusively in the silicates if the metal migrates as a diapir. In this limit, the diapir velocity is well approximated by the Stokes velocity (Equation 7). The metal to silicates heat flux then depends on the Péclet number (comparing advective heat transfert to diffusive heat transfer)

$$Pe = \frac{v_d R_d}{\kappa_s} \tag{12}$$

as

$$Q_{m\to s} = a 4\pi R_d^2 k_s \frac{T - T_{sm}}{R_d} Pe^{1/2}, \tag{13}$$

181 where k_s and κ_s are the thermal conductivity and diffusivity of the silicates, $a \simeq 0.46$
182 (Ulvrová et al., 2011), and T_{sm} is the temperature of the surrounding solide mantle. The
183 effect of temperature dependent viscosity will not affect significantly these laws in the
184 relevant limit of $Pe \gg 1$, because in this limit the influence of the diapir on the tem-
185 perature of the surrounding silicates is limited to a very thin thermal boundary layer (Morris,
186 1982; Ribe, 1983).

187 ### 2.2.4 Solution

As described in details in supplementary section S1, using the results of sections 2.2.2 and 2.2.3, one can write the equation governing the evolution of T (Equation 3) as

$$\frac{dT}{dP} - A(P)T = B(P), \tag{14}$$

where the two accessory functions $A(P)$ and $B(P)$ are defined as

$$A(P) = \frac{\gamma}{K_{S,m}} - 3\frac{\rho_s c_{p,s}}{\rho_m c_{p,m}} \frac{a Pe^{-\frac{1}{2}}}{\rho_s g R_d}, \tag{15}$$

$$B(P) = 3\frac{\rho_s c_{p,s}}{\rho_m c_{p,m}} \frac{a Pe^{-\frac{1}{2}}}{\rho_s g R_d} T_{sm} + \varepsilon \frac{\Delta\rho}{\rho_s \rho_m c_{p,m}}. \tag{16}$$

The solution of this equation meeting the initial condition $T(P_{\rm eq}) = T_{\rm eq}$ is (Supplementary Information S1)

$$T(P) = \left[T_{\rm eq} + \int_{P_{\rm eq}}^{P} B(P') \exp\left(\int_{P_{\rm eq}}^{P'} A(P'')dP'' \right) dP' \right] \exp\left[\int_{P_{\rm eq}}^{P} A(P')dP' \right]. \tag{17}$$

188 This expression, when applied at $P = P_{\rm CMB}(f)$, allows to obtain the temperature of
189 the metal phase when it reaches the core. Depending on the assumptions made on the
190 pressure dependence of the metal and silicates properties, the integrals can be obtained
191 analytically, or evaluated numerically.

2.3 Further compression heating within the core

Equation 17 gives the temperature of the metal when it reaches the core-mantle boundary. However, further growth of the Earth implies an additional pressure increase, with further compressional heating which has yet to be taken into account.

To estimate this effect, we assume that each metal addition stays at the same radius r in Earth's core, and has an initial pressure equal to the CMB pressure at the time at which it reached the core, *i.e.* $P(r = R_{\rm CMB}(f)) = P_{\rm CMB}(f)$. Indeed, each radius inside the core has been at some point in accretion the core radius as expressed in Table 1. Therefore, the initial pressure at these radii, before the core grew to its current size, was the pressure of the CMB after each step of accretion (the calculation of $P_{\rm CMB}(f)$ is detailed in section 3). The final pressure profile $P(r)$ in the core is estimated from a second-order polynomial approximation of the PREM model (Dziewonski & Anderson, 1981) given by:

$$P(r) = P_{center} + \left(\frac{P_{\rm CMB} - P_{center}}{R_{\rm CMB}^2} \right) r^2, \tag{18}$$

where $P_{center} = 364$ GPa is the pressure at the center of the Earth, and $R_{\rm CMB} = 3470$ km is the final radius of the Earth's core and $P_{\rm CMB}$ is the pressure at the CMB at the end of the accretion.

We assume that there is no chemical or thermal mixing between each step of core growth, a model similar to Jacobson et al. (2017). We then assume that the metal follows an isentropic path, its temperature evolving according to

$$\frac{dT}{dP} = \frac{\gamma}{K_{S,m}} T. \tag{19}$$

Integrating Equation 19 from $P = P_{\rm CMB}(f)$ to $P = P_{\rm core}(r)$ gives a temperature profile $T(r)$ which is usually not isentropic (because each diapir migrates to the core from different initial conditions) and can in principle be either stably or unstably stratified. We will then consider the possibility of having efficient radial mixing resulting in an isentropic core (see Section 5).

3 Parameterization of core/mantle segregation

The compositional constraints of our models come from previous accretion model obtained from metal/silicate high pressure partitioning of elements between metal and silicate (e.g. Siebert et al., 2012; Chi et al., 2014; Fischer et al., 2015; Clesi et al., 2016).

We base our model on the model of Fischer et al. (2015) from which we modify the parameterization of the evolution of the pressure and temperature of metal/silicate equilibration, and of the evolution of accreted material, as discussed in the following subsections. In our model, as well as in Fischer et al. (2015), the Earth is accreted in 20 steps of accretion representing 5% of the Earth mass accreted. These steps represent the average equilibrium created by impacts but are not to be mistaken for individual impacts. The step of accretion can be seen as the average equilibrium and compositional change of the core and mantle of a growing Earth, without having to model all impacts, which would require to model the entire accretion history as in Rubie et al. (2015). The pressure of equilibrium serves then as a proxy to the impact history: lower pressure at a given step means that for this step of accretion the impactors are smaller, while higher pressure at a given step of accretion means the impacts are bigger and more energetic (see for instance the scaling law of Nakajima et al., 2021). Further discussion on the why this method of continuous step accretion works in terms of bulk geochemistry can be found in the following references studying metal-silicate partitioning, among others: Wade and Wood (2005); Wood et al. (2008); Righter (2011); Tuff et al. (2011); M. Bouhifd and Jephcoat (2011); Boujibar et al. (2014); Fischer et al. (2015); Badro et al. (2018); Grewal et al. (2019).

In the following sections, we test different accretion scenario by varying the pressure of equilibrium at each step, using a parameterized equation. The scenarios tested cover a large range of accretion history, for which we only keep the scenarios yielding mantle composition close to the Bulk Silicate Earth.

3.1 Parameterization of metal/silicates equilibration conditions

3.1.1 Pressure and temperature of equilibration

The first factor controlling chemical equilibrium between metal and silicate in a magma ocean is the pressure at the base of the magma ocean. We choose to parameterize the equilibration pressure P_{eq} using a modified cumulative Weibull distribution function written as:

$$P_{\mathrm{eq}}(f) = a_P P_{\mathrm{CMB}}(f) \frac{1 - \mathrm{e}^{-(f/f_c)^\lambda}}{1 - \mathrm{e}^{-(1/f_c)^\lambda}}, \tag{20}$$

where f is the mass fraction of Earth which has been accreted, $P_{\mathrm{CMB}}(f)$ is the pressure at the core-mantle boundary (CMB), a_P a parameter setting the final equilibration pres-

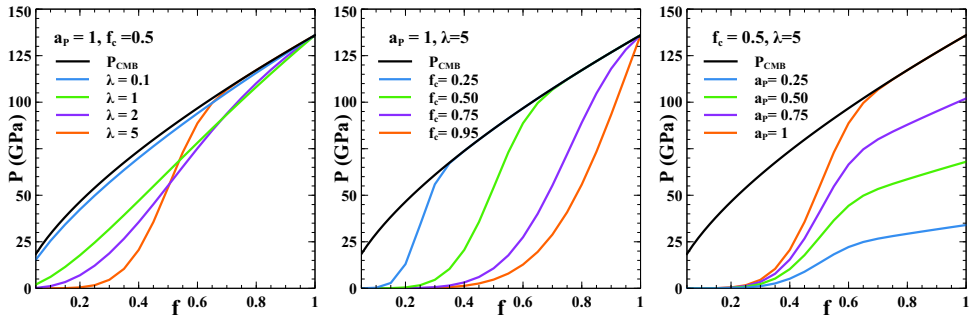

Figure 1. Variation of $P_{\rm eq}$, calculated by Equation 20, as a function of the Earth's mass fraction accreted (f) for: $a_P = 1$, $f_c = 0.5$ and varying λ values (left panel); $a_P = 1$, $\lambda = 5$ and varying f_c values (centre panel); $f_c = 0.5$, $\lambda = 5$ and varying a_P values (right panel).

sure, $P_{\rm eq}(f = 1) = a_P P_{\rm CMB}(f = 1)$; f_c and λ are the scale parameter (parameter defining both the moment in accretion when P_{eq} increase faster at high λ values and the transition from reduced to oxidized impactor) and shape parameter (parameter defining the sharpness of the transition from shallow to deep magma ocean) of the Weibull distribution function $1 - {\rm e}^{-(f/f_c)^\lambda}$. To simplify the compositional and thermal calculation, we set the equilibration pressure at each step of accretion by calculating the CMB pressure assuming an hydrostatic gradient within the Earth, following equations (2.72) and (2.73) of Turcotte and Schubert (2002):

$$P_{\rm CMB}(f) = \frac{4\pi}{3}\mathcal{G}\overline{\rho_s}(f)R_{\rm CMB}(f)^2\left[\frac{\overline{\rho_s}}{2}(f)\left(\frac{R_\oplus(f)^2}{R_{\rm CMB}(f)^2}-1\right)+\Delta\overline{\rho}\left(1-\frac{R_{\rm CMB}(f)}{R_\oplus(f)}\right)\right], \quad (21)$$

where $\mathcal{G}$ is the gravitational constant, and $R_\oplus(f)$ and $R_{\rm CMB}(f)$ are the radii of the Earth and core, both functions of mass fraction accreted, given in Table 1 . The mean densities of silicate and metal at a given step of accretion ($\overline{\rho_s}(f)$ and $\Delta\overline{\rho} = \overline{\rho_m}(f) - \overline{\rho_s}(f)$) are obtained from the mass accreted, the mass fraction of metal (and therefore silicate) accreted and the radius of the Earth and of the core: $\overline{\rho_s}(f) = m^{accreted}_{silicate}(f)/V_{\rm mantle}(f)$ and $\overline{\rho_m}(f) = m^{accreted}_{metal}(f)/V_{\rm core}(f)$. Note that the mean densities are not obtained by integration of a $P = f(\rho)$ relationship for metal or silicate, thus avoiding defining a specific equation of state for the mantle.

The parameterization defined by Equation (20) allows to vary the shape of the equilibration pressure curve $P_{eq}(f)$ as illustrated in Figure 1. With the shape parameter λ set to 0, Equation 20 reduces to $P_{\rm eq}(f) = a_P P_{\rm CMB}(f)$: the equilibration pressure is a

fixed ratio a_P of the CMB pressure, as assumed in many previous core formation models (e.g. Wood et al., 2008; M. Bouhifd & Jephcoat, 2011; Fischer et al., 2015; Rubie et al., 2015; Clesi et al., 2016). If instead $\lambda \to \infty$, the Weibull cumulative distribution function tends toward a step function equal to 0 for $f < f_c$ and 1 for $f > f_c$. In this limit, $P_{\rm eq}$ is equal to 0 for $f < f_c$ and $a_P P_{\rm CMB}(f)$ for $f > f_c$. Choosing a finite value for λ allows to vary the shape of $P_{eq}(f)$ between these two limits, as shown in Figure 1: a moderate value of λ results in a gradual increase of $P_{eq}(f)$ (see the $\lambda \leq 3$ curves in the left panel of Figure 1), while a large value of λ results in an equilibration pressure starting low and increasing sharply around $f = f_c$, before approaching the $a_P P_{\rm CMB}(f)$ curve (see the $\lambda = 5$ curves of Figure 1).

It will be convenient to discuss the results of the calculations in terms of the average equilibration pressure $\overline{P_{eq}}$, defined as

$$\overline{P_{eq}} = a_P \int_0^1 P_{\rm CMB}(f) \frac{1 - \mathrm{e}^{-(f/f_c)^\lambda}}{1 - \mathrm{e}^{-(1/f_c)^\lambda}} df. \tag{22}$$

For a given pair (f_c, λ) (i.e. the pair of parameter defining both the moment in accretion when P_{eq} increase faster at high λ values and the transition from reduced to oxidized impactor and the parameter defining the sharpness of the transition from shallow to deep magma ocean), there is a one-to-one relation between a_P and $\overline{P_{eq}}$. The evolution of $P_{eq}(f)$ is therefore fully characterized by the $(\overline{P_{eq}}, f_c, \lambda)$ triplet, which can be used in place of the (a_P, f_c, λ) triplet.

The second factor controlling the equilibrium is the temperature of equilibrium between metal and silicate and metal at the base of the magma ocean. We assume that the temperature of equilibrium is given by the liquidus temperature of the silicate from Andrault et al. (2011),

$$T_{\rm eq} = 1940 \left(\frac{P_{\rm eq}}{29} + 1 \right)^{1/1.9}, \tag{23}$$

which is higher than the liquidus of metal. Here $P_{\rm eq}$ is expressed in GPa, and $T_{\rm eq}$ in K.

3.1.2 Physical meaning of P_{eq} and T_{eq}

Following the chemical approach to mantle/core segregation, we do not go to the trouble of modeling each accretion impact. We use Equations 20 and 23 to parameterize the evolution of the equilibration conditions. As classically done in metal/silicate partitioning studies, the growth of the planet and the change in composition is discretized

in several steps of accretion, with different step sizes corresponding to different percentage of mass added to the planet (a non exhaustive list of this kind of model can be found in the following list, sampling different step size or approaches Wade & Wood, 2005; Wood et al., 2008; M. Bouhifd & Jephcoat, 2011; Boujibar et al., 2014; Fischer et al., 2015; Clesi et al., 2016; Suer et al., 2021). Each step represent the average of several impacts. If the impacts during one step are bigger and more energetic, then it will produce a deeper magma ocean, and therefore a higher value for P_{eq} (Tonks & Melosh, 1993; Nakajima et al., 2021). On the other hand, smaller, less energetic impacts will tend to result in a shallower magma ocean and lower values of P_{eq}. In all previous study, the accretion history is fixed prior to the calculation, while in our study we can test different accretion history by varying the depth of the magma ocean.

Figure 1 should then be read as a proxy of the impact history, through the evolution of the magma ocean. We also combine the shape parameter with the compositional shift from reduced to oxidized accretion. The justification of this shift in composition is given in Section 3.2. The main motivation for combining the shape parameter f_c (parameter defining the moment in accretion when P_{eq} increase faster at high λ values) in Equation 20 with the composition shift is to allow the model to be fully parameterized by three parameters instead of having four parameters to vary (which would multiply the number of simulation by 20). It also makes sense to use this parameter, since the increase in P_{eq} happens for $f > f_c$ at high values of λ, and is a proxy for larger impact of more evolved, more oxidized planetary embryos impacting at the end of accretion (Raymond et al., 2009; Rubie et al., 2015; Suer et al., 2021).

In Table 2, we list a summary of the physical and chemical meaning of the parameters used in Equation 20. In Section 3.2, we will explain why we chose f_c to define a shift between reduced and accreted material. This model will span a lot of different scenarios. There is some (a_P, f_c, λ) triplet values that can be directly translated into an easy understandable impact history:

- Very shallow magma ocean (low size impacts) accretion followed by giant impacts in the last 10% of accretion melting the entire mantle: $a_P = 1$, $f_c \sim 0.85 - 0.9$ and $\lambda \sim 5$

Parameter values			Magma ocean evolution	Impactor history	Main impactor composition
$a_P \sim 0.05$	$f_c \sim 0.05$	$\lambda \sim 0$	shallow magma ocean, smooth increase	small impacts only	Oxidized
$a_P \sim 0.05$	$f_c \sim 0.05$	$\lambda \sim 5$	shallow magma ocean, sharp increase at the end	small impacts, a bit bigger at the end	Oxidized
$a_P \sim 0.05$	$f_c \sim 1$	$\lambda \sim 0$	shallow magma ocean, smooth increase	small impacts only	Reduced
$a_P \sim 0.05$	$f_c \sim 1$	$\lambda \sim 5$	shallow magma ocean, sharp increase at the end	small impacts, a bit bigger at the end	Reduced
$a_P \sim 1$	$f_c \sim 0.05$	$\lambda \sim 0$	deep magma ocean, smooth increase	medium size impact all along	Oxidized
$a_P \sim 1$	$f_c \sim 0.05$	$\lambda \sim 5$	shallow first, sharp transition to deep at the beginning	small first, get larger early in the accretion history	Oxidized
$a_P \sim 1$	$f_c \sim 1$	$\lambda \sim 0$	deep magma ocean, smooth increase	large impactors	Reduced
$a_P \sim 1$	$f_c \sim 1$	$\lambda \sim 5$	shallow first, sharp transition to deep toward the end	small first, large at the end	Reduced

Table 2. Physical and chemical meaning of the main combination of the parameters controlling Equation 20. This is a qualitative description, assuming the size of impactors controls the magma ocean depth. The effect described can be seen also in Figure 1.

- Small step accretion, followed by intermediate size impactors finalized by the Moon forming impact melting more than 75% of the mantle (Suer et al., 2021): $a_P > 0.75$, $f_c \sim 0.8$, $\lambda \sim 5$
- The original Fischer et al. (2015) model on which this study is based: $a_P \sim 0.5-0.75$, $f_c = 0.75$, $\lambda = 0$
- Steady increase of the magma ocean depth at 50% of P_{CMB} with accretion (Boujibar et al., 2014; Clesi et al., 2016): $a_P \sim 0.5$, $f_c = 0.6 - 1$, $\lambda = 0$
- Oxidized history of accretion (Siebert et al., 2013): $a_P \sim 0.4 - 0.5$, $f_c \rightarrow 0.05$, $\lambda = 0$

A Moon forming impact effect with some metal-silicate equilibrium is modeled by the last 10% of accretion for high values of λ, f_c and a_P. An error is introduced by the fact that we extract metal in 2 steps instead of modeling one final impact corresponding to 10% of the Earth's mass.

In terms of chemical compositions and for the elements we chose to study, the error introduced by the model is not important, as the main control of the model is the concentration of Ni and Co (Fischer et al., 2015), which are not that much affected by the Moon-forming impact if there is some equilibrium between metal and silicate (Clesi et al., 2020). The error introduced for the temperature is also low, since most of the core has already acquired its heat. However, this model cannot account for core-merging events during late accretion, because by construction it needs to have some chemical equilibrium at some point.

3.2 Composition of accreted material

Following Fischer et al. (2015), we assume that the accreted material changes from reduced to oxidized at a given time in accretion. This transition from reduced to oxidized material is necessary to explain the partitioning behavior of moderately siderophile elements which depend highly on oxygen fugacity such as Nb, Ta, Cr and V (e.g. Tuff et al., 2011; Cartier, Hammouda, Doucelance, et al., 2014), as well as the sulfur behavior (Boujibar et al., 2014; Laurenz et al., 2016). It is also more coherent with dynamical accretion model and distribution of oxidized material within the early solar system(Morbidelli et al., 2000; Raymond et al., 2009; Raymond & Izidoro, 2017; Izidoro et al., 2021). While in Fischer et al. (2015)'s model this change is assumed to occur when 75% of Earth's mass

has been accreted, we here vary this time from a calculation to the other, assuming it happens at the accreted fraction f_c defined in the parameterization of the equilibration pressure (Equation (20)). The composition of the accreting material is derived from CI chondrites composition (Wasson & Kallemeyn, 1988) equilibrated for different oxygen fugacity, thus ensuring that refractory lithophile element concentrations will be close to the chondritic trend (for a full explanation of this choice, see Fischer et al. (2015) and references therein). The composition of accreting impactors is given in Table 3.

3.3 Compositional model

3.3.1 Calculation of equilibrium compositions

The equilibrium is set by reaction of an oxide $MO_{n/2}$ in the magma ocean transforming into a metal M in the metallic phase. This reaction is written:

$$MO^{m.o.}_{n/2} + \frac{n}{2}Fe^m \rightarrow M^m + \frac{n}{2}FeO^{m.o.} \tag{24}$$

where $MO^{m.o.}_{n/2}$ is the oxide in the silicate liquid (magma ocean) and M^m is the same element in its metallic form in the liquid metal alloy. The equilibrium constant of this reaction defines the exchange partitioning coefficient for element M, K_d^M. By combining Equations 20 and 23 it is possible to calculate the partitioning behavior between the liquid metal and the liquid silicate of moderately siderophile elements using the exchange partitioning coefficient K_d^M of element M (Ni, Co, Si, V, Cr or O), using the parametrization

$$log_{10}K_d^M = a_M + \frac{b_M}{T_{\rm eq}} + \frac{c_M P_{\rm eq}}{T_{\rm eq}}, \tag{25}$$

where $P_{\rm eq}$ is expressed in GPa, $T_{\rm eq}$ in K. We use values of a_M, b_M and c_M obtained experimentally by Fischer et al. (2015). The exchange partitioning coefficient for an element M of valence n is given by:

$$K_d^M = \frac{\chi^m_M}{\chi^{m.o.}_{MO_{n/2}}} \left(\frac{\chi^{m.o.}_{FeO}}{\chi^m_{Fe}} \right)^{n/2}. \tag{26}$$

where χ^m_M is the molar fraction of element M in the liquid metal, and $\chi^{m.o.}_{MO_{n/2}}$ is the molar fraction of the corresponding oxide in the silicate liquid. At each impact the mass of silicate and metal accreted are equilibrated with each other at a pressure and temperature defined by Equations 20 and 23, which yields the partitioning behavior of moderately siderophile elements (Equation 25) at a given step of accretion and for given values of a_P, f_c (parameter defining both the moment in accretion when P_{eq} increase faster

Elements	Reduced material	Oxidized material
Silicate phase		
SiO_2	51.41	42.19
MgO	37.5	29.40
Al_2O_3	4.62	3.63
CaO	3.75	2.95
FeO	2.24	21.13
NiO (ppm)	10.1	174
CoO (ppm)	5.1	83
Cr_2O_3 (ppm)	4500	6170
V_2O_3 (ppm)	203	164
Metallic phase		
Fe	91.1	89.07
Ni	5.55	10.0
Co	0.26	0.34
Si	2.4	0.0205
Cr (ppm)	6100	870
V (ppm)	9.24	0.775
O	0.04	0.4
Metallic mass fraction of the impactor		
-	0.313	0.165

Table 3. Impactor composition given in Fischer et al. (2015) supplementary material and used in our model. All units are in wt % except where ppm is specified.

at high λ values and the transition from reduced to oxidized impactor) and λ (parameter defining the sharpness of the transition from shallow to deep magma ocean). The composition of the metallic phase accreted to the core is set by mass balance equations and partitioning behavior. The mass balance is derived from the technique described in the supplementary materials of Rubie et al. (2011), with a few modifications. The detail of the calculation is given in the Supplementary Information S2.

3.3.2 Final compositions

After each impact, we obtain the composition of the masses of metal and silicate that are added to the core and the mantle respectively. These compositions are not representative of the bulk evolution of the core and mantle, the latter being set by the cumulative effects of all the impacts. The composition and temperature of the metal added to the core evolves as accretion proceeds, as a result of the evolution of the equilibration conditions and composition of the mantle. This implies that the core could end up being chemically and thermally stratified. This stratification is likely stable, since the equilibration conditions are likely to evolve toward higher temperature and pressure as the size of the planet increases, which helps incorporating light elements such as O and Si. Some degree of radial mixing may happen however, either when the metal is added the core (Landeau et al., 2016), or because of the possibly intense stirring induced by giant impacts (Jacobson et al., 2017). In what follows, we will consider two end-member scenarios assuming either no mixing, resulting in a compositionally and thermally stratified core, or perfect mixing, resulting in a homogeneous and isentropic core.

In the following, we will be dealing with the bulk composition of the mantle only, neglecting any heterogeneities in the mantle. On the other hand, we will refer to both stratified core concentrations and bulk core concentrations, which will be indicated by the super script *strati* or *bulk* respectively.

The discirimination of the results is made by comparing the final bulk mantle composition of the model to the Bulk Silicate Earth (BSE) composition given in McDonough and Sun (1995). To calculate the final bulk composition we use an iterative approach, evolving the silicates composition according to

$$\chi^{s+}_{i,\mathrm{bulk}}(f) = \frac{\chi^{s}_{i}(f) m^{s}_{\mathrm{accreted}}(f) + \chi^{s-}_{i,\mathrm{bulk}} M^{-}_{\mathrm{mantle}}}{M^{+}_{\mathrm{mantle}}} \tag{27}$$

where $\chi^{s-}_{i,\mathrm{bulk}}(f)$ and $\chi^{s+}_{i,\mathrm{bulk}}(f)$ are the bulk concentrations before and after the impact, and M^{-}_{mantle} and M^{+}_{mantle} the masses of the mantle before and after the impact ($M^{+}_{\mathrm{mantle}} = M^{-}_{\mathrm{mantle}} + m^{s}_{\mathrm{accreted}}(f)$). With Equation 27, we obtain $\chi^{s}_{i,\mathrm{bulk}}(f = 1)$ which is the BSE concentration for a given element. The same equation can be used with $m^{m}_{\mathrm{accreted}}(f)$ and $M_{\mathrm{core}}(f - 1)$ to calculate the bulk composition of the core.

4 Simplifying hypothesis for the temperature profile calculation

The metallic alloy is initially set at the same temperature as the silicate at the bottom of the magma ocean, where it acquire its composition. This temperature is given by Equation 23, and is straightforward to calculate as it depends only on the equilibrium pressure set by Equation 20. Then the metal forms a diapir and goes through the solid mantle to reach the CMB and form the core, following Equation 17. Finally, the metal forming the core undergoes an isentropic compression as the core grows, following Equation 19. To solve EquationS 17 and 19 we need some simplifying hypothesis that are presented in this section. The choices made in this section are discussed in detail in Section 7.1.

4.1 Equation of state of liquid metal

The choice of an equation of state (EOS) for the metal is key here. The EOS has to be realistic, taking into account the effect of pressure and composition, while mathematically simple enough to obtain closed form solutions of equations 17 and 19. Our strategy is to first obtain an EOS for pure iron, and then add a correction accounting for the effect of composition. Our EOS has to describe accurately the evolution of the density along a constant entropy compression path, since deviations from this path during the migration of a diapir are expected to be small (as argued in section 2.2.2). The target property is therefore $K_{S,m}(P)$. To constrain the EOS, we use the present-day density profile in the core according to the PREM model, as well as experimental and *ab initio* estimates of the density of pure iron and iron alloys at various pressures and temperatures. One advantage of using PREM as a constraint is that we can reasonably assume that the core is close to isentropic and chemically homogeneous, which implies that the evolution of density with pressure in the core is a good measure of isentropic compression. Since in addition K_S is usually a weak function of temperature (Ichikawa et al., 2014; Kuwayama et al., 2020), the pressure dependence obtained from PREM should

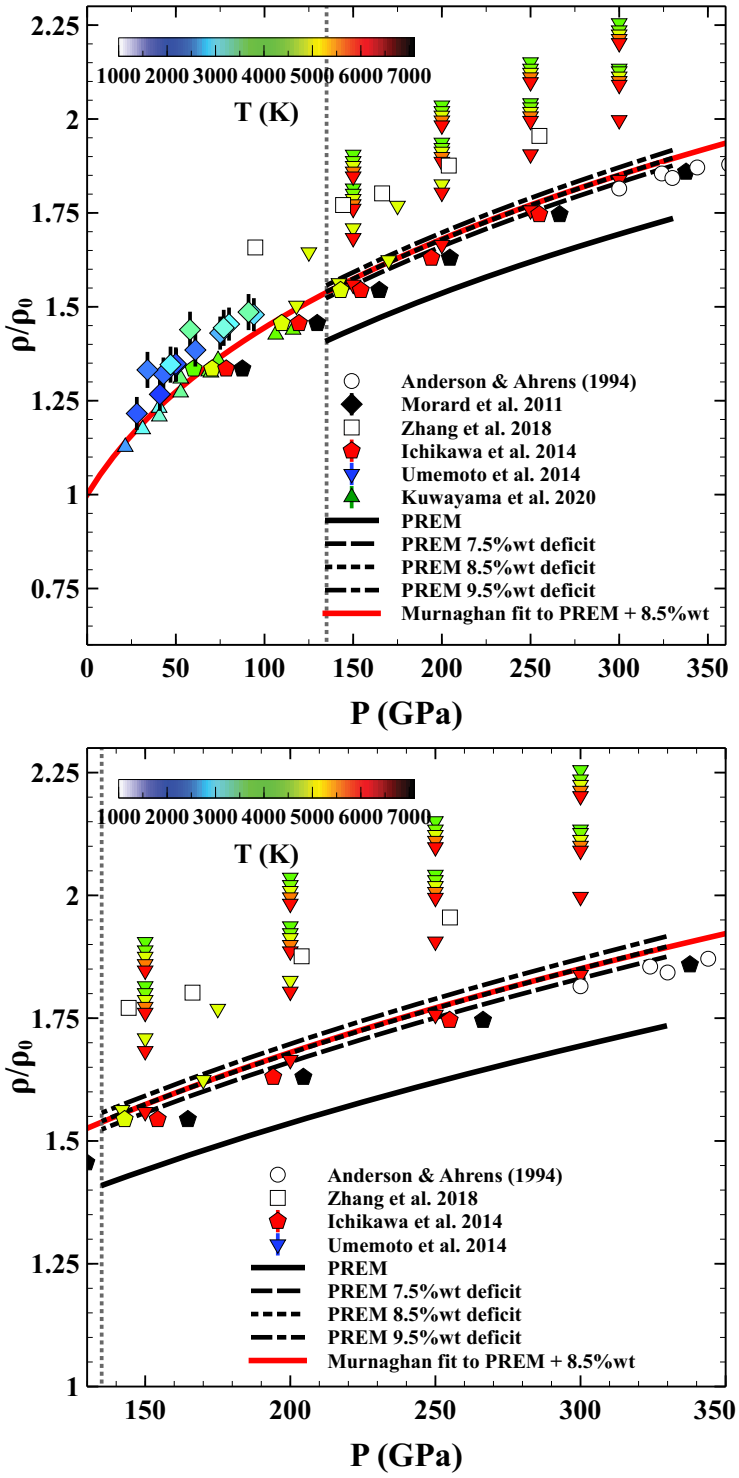

Figure 2. Different equations of state for liquid metal and experimental and ab initio data. On the left, data covering the whole P-space relevant for Earth formation. On the right, close-up on the core conditions. The color scale indicate the temperature of experimental (Morard et al., 2013; Kuwayama et al., 2020) and ab inito data (Umemoto et al., 2014; Ichikawa et al., 2014), the white symbols are 300 K data points of Anderson and Ahrens (1994) and Zhang et al. (2018)). PREM model and its variations are the black lines (PREM for iron: solid, 7.5%wt density deficit: dashed line, 8.5%wt density deficit: dotted line, 9.5%wt density deficit: dotted-dashed line). The red line is a fit of the Murnaghan equation of state used for this study.

be rather robust. In contrast, the (P, T) conditions of individual experiments and calculations, when taken collectively, do not follow isentropic compression paths, which makes difficult to extract a parametrization for $K_{S,m}(P)$. Earth's core is not made of pure iron, however, and the density profile from PREM therefore has to be corrected for the presence of light elements. Figure 2 shows the data used to constrain the EOS, which include PREM's density profile and experimental and *ab initio* estimates for various compositions. In order to highlight the effect of pressure, we normalize the density $\rho(P)$ of each data point by the density ρ_0 at low pressure and same composition. The density from PREM is corrected by assuming that the core is 7.5%, 8.5%, or 9.5% less dense than pure iron, to account for the presence of light elements.

We have tried several parametrisations for our EOS, and found that a simple Murnaghan equation of state (Murnaghan, 1944) allows to match satisfactorily the composition-corrected density profile from PREM (density deficit of 8.5%) and the experimental and *ab initio* data. The Murnaghan equation of state assumes that the isentropic bulk modulus is a linear function of P,

$$K_{S,m} = K_0 + K'P, \tag{28}$$

where K_0 is the bulk modulus at zero pressure and K' its derivative with respect to pressure. Integration of the relation $K_{S,m} = \rho\frac{\partial P}{\partial \rho}$ over ρ yields

$$\frac{\rho_m(P)}{\rho_0} = \left(1 + \frac{K'}{K_0}P\right)^{1/K'}. \tag{29}$$

Assuming that the core is 8.5% less dense than pure iron, we find that the Murnaghan equation adequately describes the corrected PREM profile and lower pressure data with $K_0 = 128.49$ GPa and $K' = 3.67$ (red curve on Figure 2). In our model, the metal is a Fe-Ni-Co-Si-O-V-Cr alloy, and the effect of composition on ρ_0 is obtained as follows:

$$\rho_0 = \left(\chi^m_{Fe}\rho_0^{Fe} + \chi^m_{Ni}\rho_0^{Ni} + \chi^m_{Co}\rho_0^{Co} + \chi^m_{V}\rho_0^{V} + \chi^m_{Cr}\rho_0^{Cr}\right)\exp\left(\alpha_{Si}\chi^m_{Si} + \alpha_O\chi^m_O\right), \tag{30}$$

where $\alpha_{Si} = -0.91$ and $\alpha_O = -1.8$ are the expansion coefficient of Si and O in metallic alloys. The values ρ_0^i are given in Table 4.1. Equation 30 is calculated assuming the transitions metals (Ni,Co, V and Cr) are replacing Fe atoms in the alloy, and therefore change the mass without changing the volume. For non-metallic elements (Si and O), the volume and the mass are changed, as shown by Alfè et al. (2002), therefore their effect on density has to be taken into account through the expansion coefficient (the exponential factor in Equation 30). The full demonstration of the formula is given in Appendix A of Deguen and Cardin (2011). By including Equation 30 into Equation 29, we

ρ_0^{Fe}	ρ_0^{Ni}	ρ_0^{Co}	ρ_0^{V}	ρ_0^{Cr}	α_{Si}	α_O
7019	7900	8900	6100	7190	-0.91	-1.8

Table 4. Values of ρ_0^i in kg.m^{-3} and expansion coefficient for light elements (Si and O) used in equation 30. The expansion coefficient are taken from Deguen and Cardin (2011) and references therein. Iron value is from (Anderson & Ahrens, 1994) while the other element are from thermodynamic tables

get an equation of state that take into account pressure dependency (through Equation 29) and compositionnal dependency (through Equation 30).

4.2 Compression-driven heating

We first consider the case where $Pe \to \infty$ and $\varepsilon = 0$. This means that the diffusion of temperature between the metal and the surrounding mantle is negligible and that the gravitational energy dissipation happens in the mantle only. In these conditions, $A(P) = -\frac{\gamma}{K_{S,m}}$, $B(P) = 0$, and Equation 17 simplifies to Equation 19. To solve this equation we need the evolution of the Grüneisen parameter with pressure. We use the equation of Al'Tshuler et al. (1987):

$$\gamma(P) = \gamma_\infty + (\gamma_0 - \gamma_\infty)\left(\frac{\rho_0}{\rho_m}\right)^\beta, \tag{31}$$

with $\gamma_\infty = 1.305$, $\gamma_0 = 1.875$ and $\beta = \gamma_0/(\gamma_0 - \gamma_\infty)$ (values from Dewaele et al., 2006). When combining Equations 31 and 28 in Equation 19, it is possible to integrate the equation and have an analytical solution given by

$$T(P) = T_{\text{eq}}\left(\frac{\rho_m(P)}{\rho_m(P_{\text{eq}})}\right)^{\gamma_\infty} \exp\left[\frac{\gamma_0 - \gamma_\infty}{\beta}\left(\left(\frac{\rho_0}{\rho_m(P_{\text{eq}})}\right)^\beta - \left(\frac{\rho_0}{\rho_m(P)}\right)^\beta\right)\right], \tag{32}$$

where $P(r)$ is the final pressure in the core at radius r (Equation 18). The ratio $\frac{\rho_0}{\rho_m}$ is given by Equation 29.

4.3 Dissipation of gravitational energy

In the previous section, both dissipation and diffusion terms were set to zero. Here we still assume that $Pe \to \infty$, but now examine the case where some fraction ϵ of dissipative heating does heat the metal. While ε is likely very small if the metal migrates

as a diapir (section 2.2.2), it may not be so if the metal migrates by percolating through the mantle.

We do not calculate directly the dissipation, but rather test several fixed values of ε between 0 and 1. In this case, Equation 17, using Equation 31, becomes

$$\begin{aligned} T(P_{\rm CMB}(f)) \quad = \quad & \left(\frac{\rho_m(P_{\rm CMB})}{\rho_m(P_{\rm eq})}\right)^{\gamma_\infty} \exp\left[\frac{\gamma_0-\gamma_\infty}{\beta}\left(\left(\frac{\rho_0}{\rho_m(P_{\rm eq})}\right)^{\beta}-\left(\frac{\rho_0}{\rho_m(P_{\rm CMB})}\right)^{\beta}\right)\right]\times \\ & \left[T_{\rm eq}+\varepsilon C_{p,m}\int_{P_{\rm eq}}^{P_{\rm CMB}}\left(\frac{1}{\rho_s}-\frac{1}{\rho_m(P')}\right)\left(\frac{\rho_m(P')}{\rho_m(P_{\rm eq})}\right)^{\gamma_\infty}\times\right. \\ & \left.\exp\left\{\frac{\gamma_0-\gamma_\infty}{\beta}\left(\left(\frac{\rho_0}{\rho_m(P_{\rm eq})}\right)^{\beta}-\left(\frac{\rho_0}{\rho_m(P')}\right)^{\beta}\right)\right\}dP'\right], \end{aligned} \tag{33}$$

which is solved numerically, with $\rho_s(f)$ being calculated at each accretion step in the same way as in Equation 21.

5 Core heat content and CMB temperature

5.1 Calculation of heat content and isentropic temperature

Once the core temperature and density profiles at the end of accretion have been obtained, we calculate the heat content of the core ($Q_{\rm core}$) right after the accretion as

$$Q_{\rm core} = \iiint \rho_m c_{p,m} T dV. \tag{34}$$

From this we estimate the isentropic temperature profile corresponding to the same heat content, assuming that the core has been thoroughly mixed, possibly as a result of mechanical stirring associated with planetary impacts or convection. This results in a chemically homogeneous (rather than chemically stratified) core, with composition obtained from Equation 27. $\rho_m(r)$ is then recalculated using Equation 29 and the final core pressure given by Equation 18. The isentropic profile is calculated from

$$\left(\frac{\partial \ln T}{\partial \ln \rho_m}\right)_s = \gamma, \tag{35}$$

which gives

$$T^{\rm is}(r) = T^{\rm is}_{\rm CMB}\left(\frac{\rho_m(r)}{\rho_{\rm CMB}}\right)^{\gamma_\infty} \exp\left[\frac{\gamma_0-\gamma_\infty}{\beta}\left(\left(\frac{\rho_0}{\rho_{\rm CMB}}\right)^{\beta}-\left(\frac{\rho_0}{\rho_m(r')}\right)^{\beta}\right)\right]. \tag{36}$$

The key parameter to be determined is the CMB temperature ($T^{\rm is}_{\rm CMB}$). Combining Equation 34 and Equation 36 gives

$$T^{\rm is}_{\rm CMB} = \frac{Q_{\rm core}}{4\pi\rho_{\rm CMB}c_{p,m}}\left[\int_0^{R_{\rm CMB}}\left(\frac{\rho_m(r)}{\rho_{\rm CMB}}\right)^{\gamma_\infty+1}\exp\left(\frac{\gamma_0-\gamma_\infty}{\beta}\left(\left(\frac{\rho_0}{\rho_{\rm CMB}}\right)^{\beta}-\left(\frac{\rho_0}{\rho_m(r)}\right)^{\beta}\right)\right)r^2dr\right]^{-1}, \quad (37)$$

which is evaluated numerically. In this equation, ρ_{CMB} is the density of the core at the CMB, determined after isentropic mixing by Equation 29.

Perfect mixing of the core is clearly not guaranteed, but the CMB temperature obtained through the procedure described above is at least a convenient measure of the thermal state of the core at the end of core formation.

5.2 Effect of the accretion parameters on the core thermal state

We now discuss the effect of the parameters a_P, λ (parameter defining the sharpness of the transition from shallow to deep magma ocean), and f_c (parameter defining both the moment in accretion when P_{eq} increase faster at high λ values and the transition from reduced to oxidized impactor)of the equilibration pressure parametrization on the post-mixing temperature of the core. As an example, we discuss a simple model in which the composition of the metal added to the core changes at $f = f_c$, from pure iron with $\rho_0 = 7019$ kg.m^{-3} (Anderson & Ahrens, 1994) for $f < f_c$ to an iron alloy with $\rho_0 = 6318$ kg.m^{-3} (10% lighter than pure iron) for the second part of accretion ($f > f_c$). As a reminder, the effect of theses parameters on the evolution of the equilibration pressure as a function of f are shown in Figure 1.

Figure 3 illustrates the three steps of our model:

(i) The first column shows the evolution of the P, T conditions of the metal phase while it migrates from the base of the magma ocean to the CMB at time of each core-forming event. We assume here negligible heat transfer between the metal and surrounding mantle, and no dissipative heating of the metal.

On the different panels are shown the silicates liquidus (black line, Equation 23), which gives the P, T conditions from which each metal addition starts its migration through the mantle.

The orange arrows show the paths of individual metal masses migrating as diapirs from two different pressures, corresponding to different magma ocean depths (blue cir-

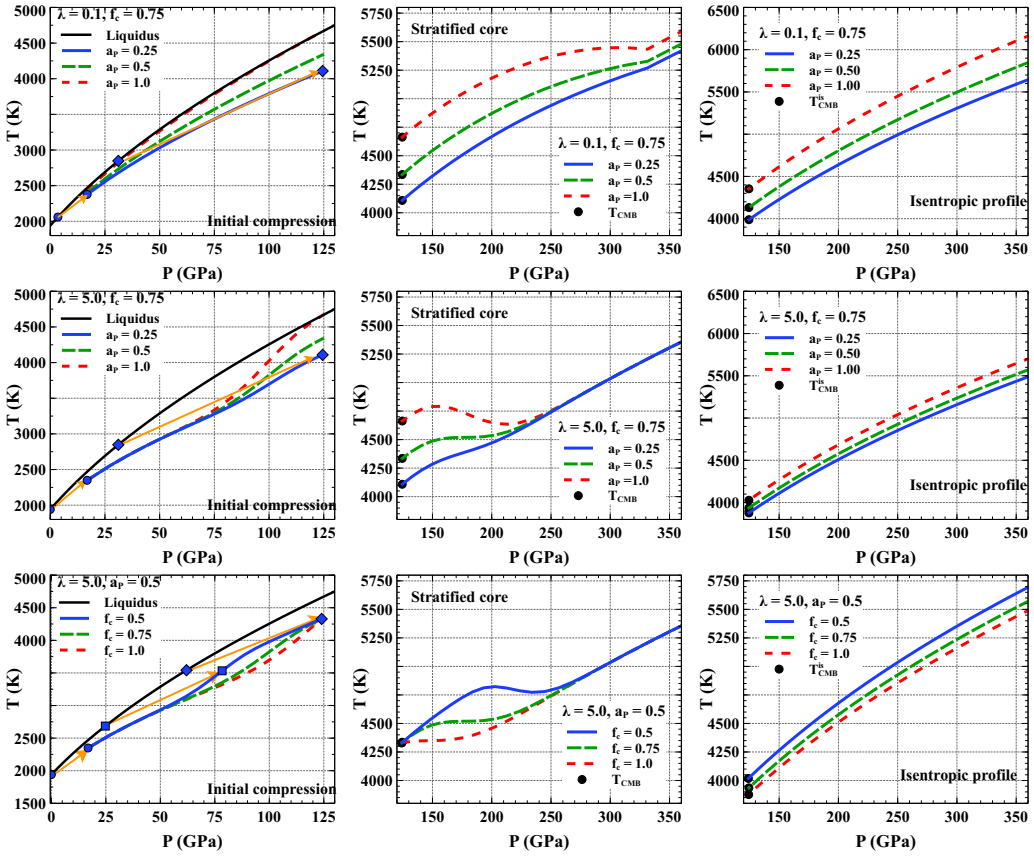

Figure 3. Summary of the different steps of the calculation for an example model mixing pure iron and a 10% lighter iron alloy. The first column describes the adiabatic compression between the base of the magma ocean and the CMB, the second column shows the temperature profile that is then used to calculate the heat content. The third column shows the fully mixed isentropic profile. The first row shows the effect of a_P, for $\lambda = 0.1$ and $f_c = 0.75$. The second row shows the effect of a_P for $\lambda = 5$ and $f_c = 0.75$. The third row shows the effect of f_c for $a_P = 0.5$ and $\lambda = 5$. The orange arrows in the first column shows the adiabatic compression path for a few points in accretion: beginning of accretion (circles), middle of accretion (squares in the third row) and end of accretion (diamonds).

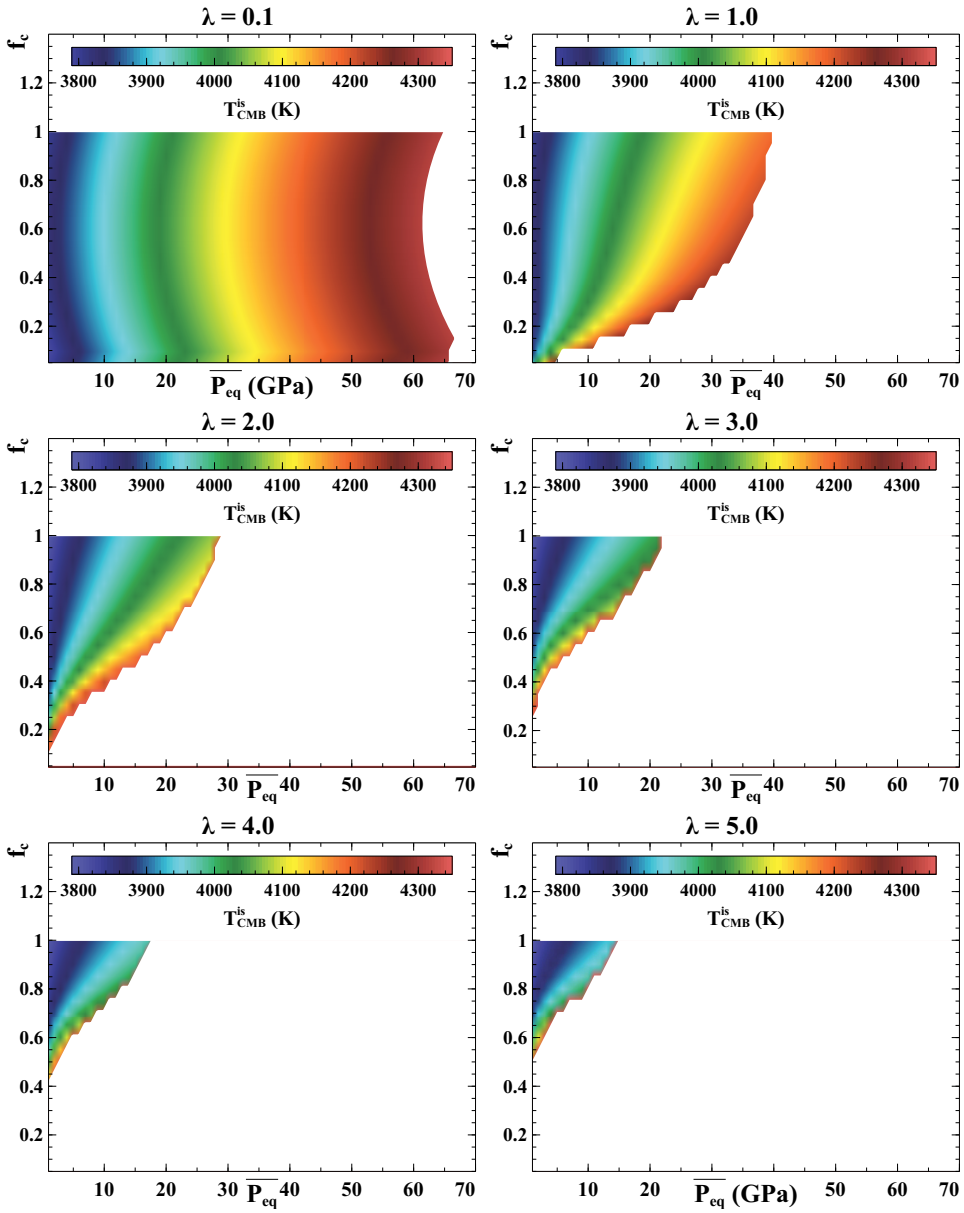

Figure 4. CMB temperature for a post-mixing isentropic core (color scale) for a mix of pure iron core and an iron alloy 10% lighter than pure iron, as a function of parameter $\overline{P_{eq}}$ (x-axis) and f_c (y-axis), for different values of λ (from left to right and top to bottom: $\lambda = 0.1$, 1, 2, 3, 4 and 5). The white areas correspond to the value of $\overline{P_{eq}}$ for a given (f_c, λ) cannot be reached for $a_P \leq 1$. The physical and chemical meaning of the parameter is explained in Section 3.1.2 and in Table 2.

cles). The final pressure of theses paths (blue diamond) is the CMB pressure at the time of metal migration. The red, green, and blue lines show the P, T conditions of metal masses originating from different magma ocean depths at the end of their migration through the mantle, for various evolutions of the magma ocean depth (different values of λ, f_c, and a_P). The lower pressures correspond to metal masses accreted early, when the Earth was still small and the CMB pressure low, while higher pressures correspond to metal masses accreted at the end of Earth's formation.

A key point here is that the adiabatic path $T(P)$ of the metal phase happens to be less steep than the silicates liquidus. As illustrated in the figures, this implies that a mass of metal starting from a deeper (higher pressure) magma ocean reaches, at the same pressure, a higher temperature than a metal mass originating from a shallower magma ocean.

It also implies that, under these assumptions, the temperature of the core at the CMB cannot exceed the liquidus of the silicates (estimated at the BSE composition).

(ii) The second column shows the temperature in the core at the end of accretion, assuming no radial mixing.

This is obtained from the temperature profiles of the first column by taking into account the additional compression associated with the growth of the planet, from the CMB pressure at the time of each metal mass addition to the pressure of the same metal mass when the core is fully formed (Equation 18). The composition of each metal mass addition is conserved. The core heat content Q_{core} is calculated from this temperature profile, using Equation 34.

(iii) The third column shows the isentropic temperature profiles obtained with the assumption of perfect mixing of the temperature profiles shown in the second column, using the procedure described in section 5.1. The CMB temperatures in the second and third columns are marked by black circles. In the following, we will focus on the isentropic CMB temperature (third column in Figure 3), but it is interesting to note that the temperature at the CMB before radial mixing (stratified profile) is different, and usually higher, than the CMB temperature of the corresponding isentropic profile.

The effect of each of the accretion parameters ($\overline{P_{eq}}, \lambda, f_c$) with $a_P < 1$ on the CMB temperature after core mixing is shown in Figure 4. Overall, the effect of these three parameters can be understood through their effects on the average pressure of equilibra-

tion. As explained in point (i) above, a higher pressure of equilibration results in a higher core temperature, a consequence of the adiabatic path $T(P)$ of the metal being less steep than the silicates liquidus. Increasing a_P (final equilibration pressure) at fixed f_c and λ increases on average the equilibration pressure, and therefore increases the core temperature. Increasing f_c (parameter defining both the moment in accretion when P_{eq} increase faster at high λ values and the transition from reduced to oxidized impactor) at fixed a_P and λ results in a lower pressure of equilibration at $f < f_c$, which results in a lower core temperature; this is significant only if λ is sufficiently large, since f_c has a negligible effect on the shape of the equilibration curve at small λ (see Figure 1). Increasing λ (parameter defining the sharpness of the transition from shallow to deep magma ocean) at fixed a_P and f_c decreases the core temperature, by lowering the equilibration pressure at $f < f_c$. Overall, for a given composition the temperature variations are within a 600 K range in this simplified model.

6 Core composition and temperature from geochemically consistent accretion models

We now discuss the state of the core resulting from equilibration paths leading to a geochemically consistent mantle composition. We start with an initial population of metal/silicates equilibration paths $(P_{eq}(f), T_{eq}(f))$ defined by triplets (a_P, f_c, λ) or, equivalently, $(\overline{P_{eq}}, f_c, \lambda)$. The mantle composition is calculated for each of these equilibration paths, and compared to the BSE composition model of McDonough and Sun (1995). Only the equilibration paths yielding a mantle composition consistent with McDonough and Sun (1995)'s model are conserved. The core composition and thermal state at the end of accretion are then calculated for each of these geochemically consistent equilibration paths, using the procedures described in the previous sections.

6.1 Mantle composition

We use a discriminating parameter $\delta^{\overline{BSE}}\chi < 10\%$ for which the calculation is described in Supplementary Information S3, in particular in Figure S3 and Table S3. By definition of this parameter, all the solutions are close enough to the BSE model of McDonough and Sun (1995) and most of the concentrations, especially the light elements, are within a 10% range of the BSE. The top panels of Figure 5 show the output (i.e. composition

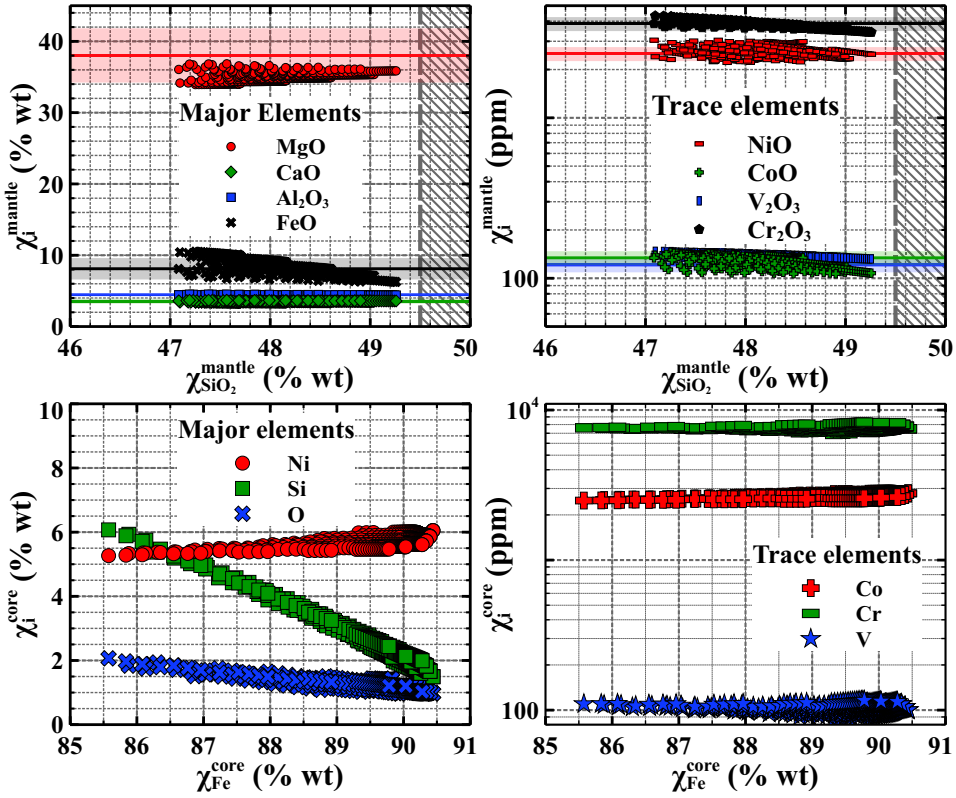

Figure 5. **Top**: Oxides concentrations in the mantle (major elements on the left, trace elements on the right) as functions of SiO_2 abundance, from accretion histories yielding $\delta^{\overline{BSE}}\chi < 10\%$. The colored solid lines represent the BSE concentrations in the reference model, with a 10% variation. The grey vertical line is the upper limit of $\chi^{BSE}_{SiO_2} \pm 10\%$. **Bottom**: Composition of the core (major elements on the left, trace elements on the right) as a function of Fe abundance, from accretion histories yielding $\delta^{\overline{BSE}}\chi < 10\%$.

that meet the requirement $\delta^{\overline{BSE}}\chi < 10\%$) mantle composition range compared to the reference model.

6.2 Geochemically consistent equilibration paths

The geochemical filter we apply to the core-formation model selects a subset of triplets (a_P, f_c, λ) – or, equivalently, $(\overline{P_{eq}}, f_c, \lambda)$ – which defines equilibration paths $(P_{eq}(f), T_{eq}(f))$ giving a mantle composition that is consistent with Earth's mantle composition. For clarity, in the rest of the text we will use $\overline{P_{eq}}$ instead of a_P. $\overline{P_{eq}}$ being indicative of the overall equilibrium pressure, while a_P is only representative of the pressure at the end of accretion. Within this subset, the parameters are correlated, as shown by the correlation

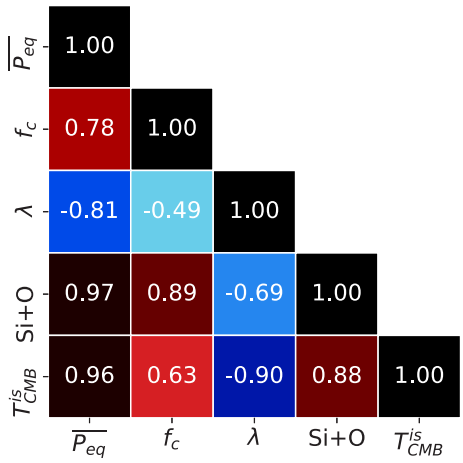

Figure 6. Correlation matrix of the variables $\overline{P_{eq}}$, f_c, λ, Si+O concentration (% wt.), and CMB temperature after core mixing, calculated from the accretion histories yielding $\delta^{\overline{BSE}}\chi < 10\%$. The physical and chemical meaning of the parameters is explained in Section 3.1.2 and in Table 2.

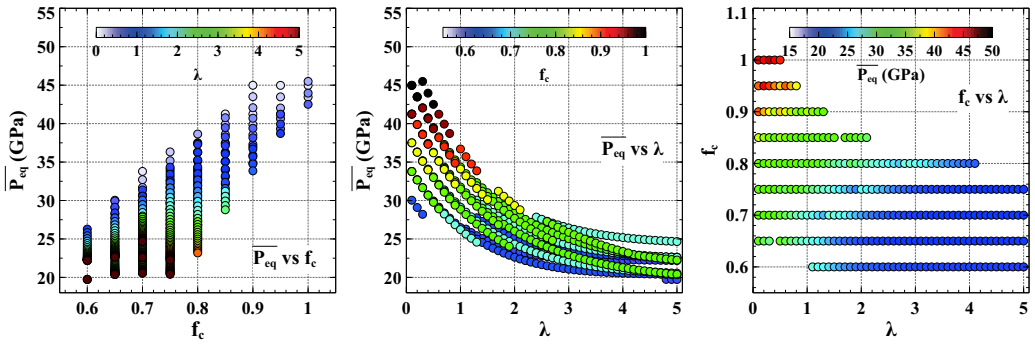

Figure 7. Range of $(\overline{P_{eq}}, f_c, \lambda)$ triplets yielding an Earth-like BSE concentration. From left to right: $\overline{P_{eq}}$ vs f_c, $\overline{P_{eq}}$ vs λ and f_c vs λ. The color scale shows the values of the third parameter. The physical and chemical meaning of the parameters is explained in Section 3.1.2 and in Table 2.

matrix of Figure 6 and illustrated in more details in Figure 7. Changing one parameter requires changing the others so as to keep a geochemically coherent model.

The geochemical filter allows values of λ (parameter defining the sharpness of the transition from shallow to deep magma ocean) within the full range of explored values (Figure 7 and Figure S5), and is therefore not discriminating for this parameter. However, high values of λ correlate with low values of f_c (i.e more oxidized composition and a more rapid transition to a deep magma ocean) and $\overline{P_{eq}}$ (i.e. the final magma ocean depth tends to be lower at higher values of λ).

The parameters $\overline{P_{eq}}$ and f_c (parameter defining both the moment in accretion when P_{eq} increase faster at high λ values and the transition from reduced to oxidized impactor) are the most affected by the geochemical filter, since only a subrange of the sampled set yields consistent BSE compositions. Successful accretion models have $\overline{P_{eq}}$ between 20 GPa and 45 GPa, and f_c between 0.6 and 1. Higher values of f_c are compensated by higher value of $\overline{P_{eq}}$: the more reduced accretion is, the deeper the magma ocean needs to be to fit the BSE composition. For f_c values close to 1, the values of $\overline{P_{eq}}$ are always higher than 40 GPa (corresponding to a_P always higher than 0.6), and only $\lambda < 1$ can fit the BSE. Reduced accretion is therefore possible only for accretion scenarios in which a very deep magma ocean ($P_{\mathrm{eq}} > 0.6 P_{\mathrm{CMB}}$) is maintained during the entire accretion.

6.3 Core composition

The core compositions of the successful differentiation models are shown on the bottom panels of Figure 5. The range of core composition is consistent with previous models of accretion (Fischer et al., 2015; Badro et al., 2018; Clesi et al., 2016; Boujibar et al., 2014): in all cases we get Fe-Ni alloy representing $\sim 80 - 90$ % of the mass, with Si and O representing ≤ 10 % of the mass, consistent with the core density deficit allowing 10 % of light elements (Dziewonski & Anderson, 1981). This is the case particularly for the higher values of $\overline{P_{eq}}$ (40- 45 GPa, Figure 8). V, Cr and Co are trace elements that have a negligible effect on density compared to the four other elements.

The concentration of Fe ranges from 85.5% wt and 90.5%wt, while the concentration of Ni ranges from 5.2 to 6.04 %wt. The concentrations of Fe and Ni are positively correlated. The major light element in the core is found to be Si, with a concentration ranging from 1.5 to 6 % wt. Oxygen is less abundant, but not negligible, with a concen-

572 tration ranging from 0.97 to 2.0% wt. The concentrations of Si and O are positively cor-
573 related. However, Si concentration is always higher than the O concentration, which is
574 consistent with the results of Ricolleau et al. (2011) and Tsuno et al. (2013). This is ex-
575 plained by the fact that for most of accretion, while the values of K_d^{Si} are lower than the
576 values of K_d^O, the final partitioning coefficient for Si is a function of $\frac{\chi_{Fe}}{\chi_{FeO}}^2$ while the par-
577 titioning of O is dependant on $\frac{\chi_{Fe}}{\chi_{Mw}}$ with $\chi_{Fe} >> \chi_{FeO}$ and $\chi_{Mw} > \chi_{FeO}$ (Frost et
578 al., 2010). Therefore, balancing the mass when the environment is reduced tends to lower
579 the spread between the Nernst partitioning coefficient of Si and the partitioning coef-
580 ficient of O in the same P-T conditions, while the spread is bit higher for oxidized con-
581 ditions. Since χ_{SiO_2} is higher than χ_{FeO} (especially in a reduced environment), the mass
582 effect tends to favor Si in metal rather than O. An illustration of this effect where from
583 a high difference in K_d values we get lower difference in partitioning coefficient which
584 yield a favorable incorporation of Si over O in the metal is presented in Figure S2. The
585 incorporation of O is favored during oxidizing phase of accretion, but as shown in Fig-
586 ure 7, the amount of oxidized impactor always represent less than 40% of accretion ($f_c \geq$
587 0.6)

588 The correlation matrix of Figure 6 and the top panels of Figure 8 show how the
589 core composition correlates with the accretion parameters. The variations of $\overline{P_{eq}}$ explain
590 most of the variance of the core composition. This strong positive correlation simply re-
591 flects the effect of pressure on the partitioning behavior of Si and O, which become more
592 siderophile at higher pressure. The correlations between the core composition and f_c (pa-
593 rameter defining both the moment in accretion when P_{eq} increase faster at high λ val-
594 ues and the transition from reduced to oxidized impactor) and λ(parameter defining the
595 sharpness of the transition from shallow to deep magma ocean) results mostly from the
596 correlations between $\overline{P_{eq}}$, f_c and λ discussed in section 6.2, and are therefore of less sig-
597 nificance.

598 ### 6.4 Core temperature

599 #### *6.4.1 Effect of $\overline{P_{eq}}$, f_c and λ on $T_{\mathrm{CMB}}^{\mathrm{is}}$*

600 Figure 8 (bottom panel) shows $T_{\mathrm{CMB}}^{\mathrm{is}}$ as a function of $\overline{P_{eq}}$, f_c (parameter defining
601 both the moment in accretion when P_{eq} increase faster at high λ values and the tran-
602 sition from reduced to oxidized impactor) and λ (parameter defining the sharpness of

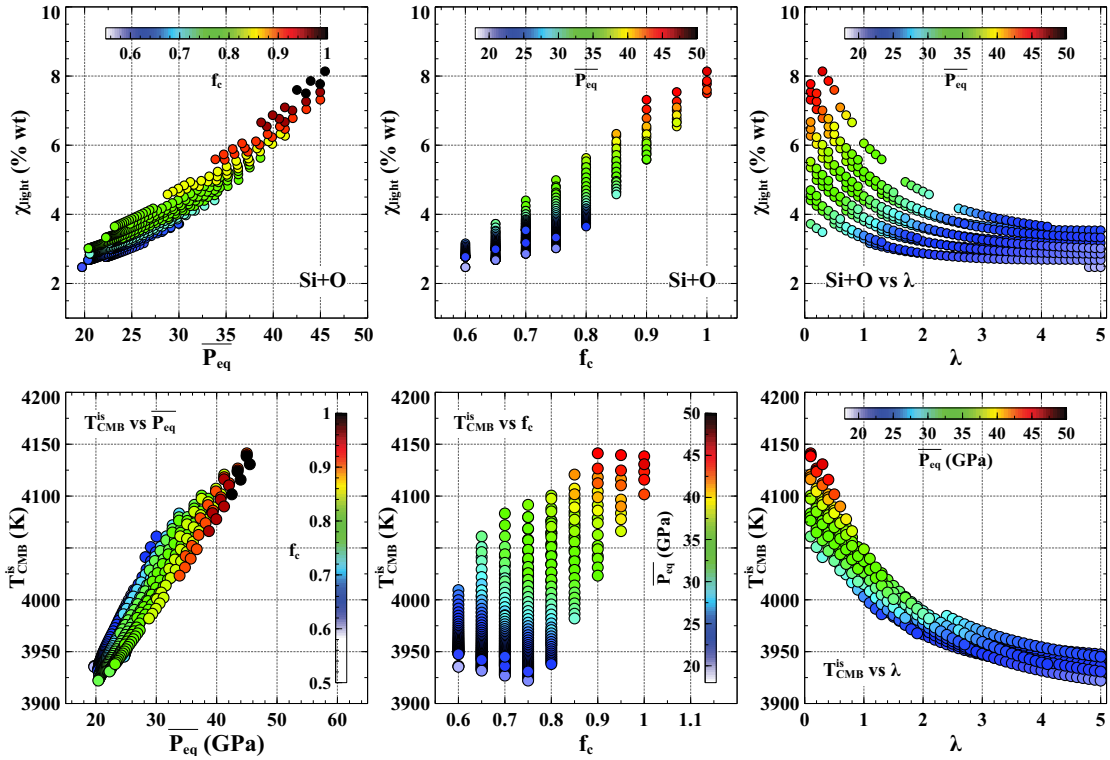

Figure 8. **Top**: Light element concentrations (O and Si in % wt) in the core as a function of a_P (left), f_c (center) and λ (right). The color scale shows the value of f_c on the left panel, and a_P on the center and right panel. **Bottom**: $T^{\text{is}}_{\text{CMB}}$ (Equation 37) as a function of $\overline{P_{eq}}$ (left), f_c (center) and λ (right). The color scale shows the values of f_c (left) and $\overline{P_{eq}}$ (centre and right) of each point. The physical and chemical meaning of the parameters is explained in Section 3.1.2 and in Table 2.

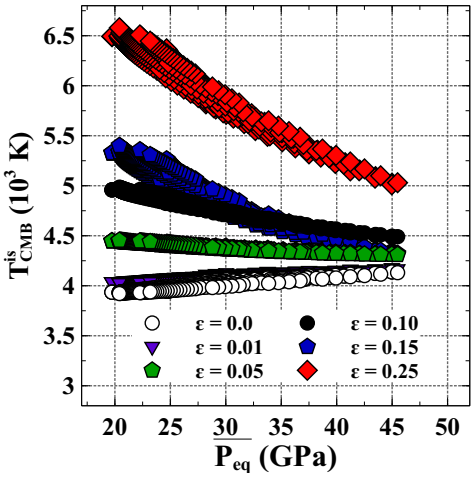

Figure 9. Value of $T^{\rm is}_{\rm CMB}$ as a function of $\overline{P_{eq}}$ for different values of ε. ε is varying between 0 and 0.25. The y-axis values are in 1000 K. The physical and chemical meaning of the parameters is explained in Section 3.1.2 and in Table 2.

the transition from shallow to deep magma ocean), assuming no dissipation in the metal phase, and negligible heat transfer between the metal and surrounding silicates. The correlation coefficients between $T^{\rm is}_{\rm CMB}$ and other parameters are given by the correlation matrix of Figure 6. The CMB temperature we obtain ranges from 3925 to 4150 K, which is consistent with some estimates the present-day CMB temperature (e.g. Nomura et al., 2014). The lowest estimate in our range is close to the present-day temperature but it should be higher because we neglected the effect of heat production elements. See Section 7.3.3 for more on the heat production.

The CMB temperature correlates positively with $\overline{P_{eq}}$, as expected from the discussion of section 5.2. The counter-intuitive positive correlation between $T^{\rm is}_{\rm CMB}$ and f_c can be explained by the positive correlation between $\overline{P_{eq}}$ and f_c among the equilibration paths consistent with the geochemical constraints. $T^{\rm is}_{\rm CMB}$ correlates negatively with λ, which is consistent with both the anti-correlation between $\overline{P_{eq}}$ and λ, and the effect of λ on the core temperature found in section 5.2. Note also the quite strong positive correlation between the temperature of the core and the abundance of Si and O.

6.4.2 Effect of dissipative heating in the metal phase

Adding dissipative heating to the metal phase during its descent through the mantle increases the core temperature as shown on Figure 9. This is a logical results of adding more heat to the metallic diapir during its descent to form the core. The final temperature profile after compression (Equation 19) is therefore calculated from an hotter temperature profile. The effect of dissipation is strongest at the lowest values of $\overline{P_{eq}}$: at $\overline{P_{eq}} =$ 20 GPa, assuming $\epsilon = 0.25$ multiplies T^{is}_{CMB} by ~ 1.6 (Figure 9) compared to the $\epsilon =$ 0 case, corresponding to temperatures up to 6500 K. At the highest value of $\overline{P_{eq}}$, the core temperature at $\varepsilon = 0.25$ is $\sim$ 1000 K higher than at $\varepsilon = 0$. The fact that dissipative heating has more effect at lower values of $\overline{P_{eq}}$ can be explained by the largest distance travelled on average by the metal through the mantle. This implies that the migration of the metal from the base of the magma ocean to the CMB induces a larger change of gravitational energy, thus resulting in more dissipative heating.

These results are consistent with the 'hot core' hypothesis (King & Olson, 2011), but are dependent on the amount of dissipation energy going into the mantle. In this study we did not focus on the mechanisms of transfer of dissipative heating, and modeled directly the amount of heat transfered to the core. However, this amount is largely dependent on the mechanism of formation, and is likely low ($\varepsilon < 15\%$). The probable values of ε is discussed further in section 7.2.

7 Discussion

The results presented in the previous section are compatible with previous estimates of the temperature at the core-mantle boundary (e.g. Nomura et al., 2014), even though our results are in the lower end of the different estimates (see for instance Labrosse, 2015, and references therein). Adding large amount of dissipation increases the core heat content, towards the hot core models, such as King and Olson (2011) model. Our model therefore shows that classical accretion models based on siderophile partitioning can be combined with thermal evolution model in order to put constraints on the heat content of the core and its subsequent evolution.

7.1 Choice of equation of state and Grüneisen parameter

The equation of state of liquid metal has a strong influence on the results. From Figure 2, we can see that a variety of equation of state for the core have been proposed.

This is due to the fact that measuring liquid metal density in high-pressure experiments (Morard et al., 2013; Sanloup et al., 2000; Kuwayama et al., 2020) is a complicated problem (hence higher error bars), and is achieved to relatively low pressure relatively to the Earth's core pressures. The ab initio data (Ichikawa et al., 2014; Umemoto et al., 2014) tend to overestimate the temperature reached in the core, yielding some error in the fit. Shock wave experiments (Anderson & Ahrens, 1994; Zhang et al., 2018) on the other hand follow an hugoniot, rendering the results harder to be reconciled with the other experimental data.

The Murnaghan equation of state we chose is closer to the PREM data for pure iron with 8.5% wt of light elements and Kuwayama et al. (2020) data, therefore getting an easy to use EOS and analytical solution. Vinet equation of state (Irving et al., 2018), or Mie-Gruneisen (Kuwayama et al., 2020) are not as simple to use and do not yield analytical solutions to our equations, while providing a very little added value for our model. Further work leading to a better understanding of the equation of state for liquid metal at higher pressure and their dependence on metal composition (especially the presence of oxygen) would be an enhancement of our models.

A second limitation to our model is the choice of Grüneisen parameter formalism. We chose to follow the formalism of Al'Tshuler et al. (1987) with the values proposed by Dewaele et al. (2006). A first limitation of this formalism is that there is no compositional dependence of the Grünesien parameter. Studies focus on pure iron (mostly solid) behaviour (Al'Tshuler et al., 1987; Dubrovinsky et al., 2000; Dewaele et al., 2006; Dorogokupets et al., 2017). These studies yield different values for γ_∞ and γ_0, between 0.9 and 1.2 and between 1.8 and 2.05 respectively (Dubrovinsky et al., 2000, and references therein). Decreasing the value of γ_∞ tend to increase the temperature of the core. This is due to a higher value of the $\gamma_0 - \gamma_\infty$, therefore leading to a higher value of T given by Equation 32. Increasing the value of γ_0 also leads to lower temperature, by increasing the value of β in Equation 32. The compositional dependency of γ_0 and γ_∞ has not been properly studied for the composition relevant to the Earth's core. The value of Dewaele et al. (2006) used in this study yield γ values relevant with pressure change: γ decreases toward γ_∞ value at higher pressures, and increases toward γ_0 value at lower pressure.

At the CMB pressure, depending on composition, $\gamma \sim 1.45$, significantly different than the constant $\gamma \sim 1.7$ used in other studies of the core (e.g. Anderson & Ahrens, 1994; Labrosse, 2015), but expected when studying the behaviour of iron at high pressure (Dubrovinsky et al., 2000).

Finally, the formalism we use to describe $\gamma(P)$ behaviour differs from the formalism adopted by Kuwayama et al. (2020): $\gamma = \gamma_0 \left(\frac{\rho_0}{\rho}\right)^b$, with $\gamma_0 = 2.02$ and $b = 0.63$. With this formalism, the ratio $\left(\frac{\rho(P)}{\rho P_{\text{eq}}}\right)^{\gamma_\infty}$ disappears from Equation 32. It yields a temperature range significantly higher than our models, between 4130 and 4280 K (see Figure S7). The discrepancy between our results and the calculation of Kuwayama et al. (2020) can be explained by the fact that their equation of state and γ formalism are fitted at the same time, yielding a value of $b = 0.63$ valid for their equation of state in the scope of their study, but that need to be refined for our conditions of calculation.

To summarize, better understanding of the equation of state of liquid metal with light elements has to be done, in parallel of a tuning of the Grüneisen parameter with the equation of state and composition of the metal. Such a combination would greatly improve our understanding of the thermal state of the core.

7.2 Range of dissipation energy transfered to the core

Our model without dissipation favors a relatively cold core, with a $T_{\text{CMB}}^{\text{is}}$ between 3925 K and 4150 K (Figure 8, bottom panels). Adding a large amount of dissipative energy to the metal phase sinking into the core can yield very high temperatures (up to 6500 K, Figure 9). However, the amount of dissipative energy transferred to the metal (ε in our model) is dependent on the mechanism of formation. When considering the likely mechanisms of core formation, the values shown in Figure 9 for $\varepsilon > 0.1$ can be seen as irrelevant, for the reasons detailed below.

One way to incorporate high amounts of dissipative energy in the metal is by the formation of a trail conduit in the silicate, which allows the dissipation energy to be transferred to small metal droplet (King & Olson, 2011). Even in this case, not 100% of the dissipative energy is transferred to the metal, with an efficiency of 60 % after King and Olson (2011), corresponding to a ε value of 0.6 in our study. In this scenario, the temperature of the core is highly dependent on the accretion style: continuous increases of the magma ocean depth ($\lambda < 1$ and $\lambda \sim 1$, $\overline{P_{eq}} > 30$ GPa), $T_{\text{CMB}}^{\text{is}}$ would be around 8

000 K; while a shallow magma ocean followed by a dramatic increase of the magma ocean depth ($\lambda > 2$, $\overline{P_{eq}} < 30$ GPa) yields temperature closer to 10 000 K. However, these temperatures are valid only if a trail conduit is formed and a substantial part of the metallic diapir is broken into droplets of 10 cm (Olson & Weeraratne, 2008). At these diapirs sizes, there is some heat loss to the mantle (see Supplementary Information S4) which would tend to lower the temperature. Furthermore, in our model we considered that all the metal is affected by the super adiabatic heating, while in the model of King and Olson (2011) only 40% of the metal is affected. If we neglect the effect of composition and apply a ratio of 40% of the metal affected by the dissipation throughout the accretion, a raw calculation gives a maximum temperature of 6000K for a global heat content 2.25 times higher than a in a non-dissipation case, those values correspond to $\varepsilon = 0.25$ and $\lambda > 4$ in our models (Figure 9). Even in a favorable case, the amount of actual dissipation energy incorporated in the metal is 25%.

If the formation of the core is happening without a trail conduit in the silicate, then the amount of dissipation energy is even lower. Core formation by diapirism favors viscous heating and dissipation of energy in the mantle rather than the metal (Ke & Solomatov, 2009; Monteux et al., 2009; Samuel et al., 2010). In this case, only a very small fraction of the dissipation energy goes into the metal (section 2.2.2). The formation of diapir by Rayleigh-Taylor instability is very efficient (e.g. Olson & Weeraratne, 2008). Therefore, it is most probable than the effect of gravitational dissipation is limited. However, even small amount of dissipative heat in the metal (5%, Figure 9) can mask the effect of the accretion style on the temperature that is discussed below.

7.3 Composition of the mantle, accretion style and core thermal state

7.3.1 Accretion style and composition

The composition of the mantle (Figure 5, top panels) yields a range of values for the parameter chosen in this study (Figures S4 and S5). In particular, the maximum pressure of equilibration (a_P) and the amount of reduced material (determined by parameter f_c) are the main parameters which have influencing the composition. Therefore, an accretion scenario fitting the BSE model has to have the following characteristics: (i) a final pressure of metal/silicate segregation between 40 and 60 % of the CMB pressure (i.e. 55 to 80 GPa, corresponding to a maximum extent of the magma ocean between

1200 and 1800 km) and an average pressure of equilibrium between 20 and 50 GPa, corresponding to a mean 25 to 60 % of the mean CMB pressure; (ii) a majority (between 60 and 80%) of the accreted material has to be reduced, with oxidized material accreting at the end of accretion. These results confirms previous studies on metal/silicate partitioning: the pressure of equilibration around 50% of P_{CMB} resulting in a magma ocean maximal depth of 1800 km, especially at the end of accretion, is a classical results necessary to explain Ni and Co abundances in the BSE (M. Bouhifd & Jephcoat, 2011; Siebert et al., 2012; Fischer et al., 2015; Badro et al., 2015). The accretion of reduced material yielded by our model is coherent with most of the studies of Earth's accretion at the exception of Siebert et al. (2013).

As shown in Figure S5, the highest number of solutions is for f_c between 0.7 and 0.8, but 30 solutions have been obtained by accreting 90 to 100% of reduced material. These solutions, especially 100% reduced accretion (n=6), are at odds with previous models (Tuff et al., 2011; Fischer et al., 2015; Rubie et al., 2015) and with the results of N-Body simulations (e.g. Morbidelli et al., 2000; O'Brien et al., 2014; Izidoro et al., 2021) which need to accrete at least some more oxidized material at the end of accretion. However, these solutions only work for $\overline{P_{eq}} > 45$ GPa ($a_P > 0.6$) and $\lambda < 1$, which means that in order to have 100% reduced impactor material, the pressure of equilibration has to be high all along the accretion. Therefore these results can be explained by the fact that oxygen fugacity tend to increase in magma with pressure (Armstrong et al., 2019, and references therein), and also by the limited number of element fitted in the model. Indeed, adding more f_{O_2} sensitive elements such as Nb and Ta (Tuff et al., 2011; Cartier, Hammouda, Doucelance, et al., 2014; Cartier, Hammouda, Boyet, et al., 2014) would have certainly help constrain the redox evolution of the planet and possibly eliminated the solutions $f_c > 0.9$, which are highly unlikely to be correct.

7.3.2 Accretion style and thermal state of the core

From Figure 8, we can see that a_P and f_c (parameter defining both the moment in accretion when P_{eq} increase faster at high λ values and the transition from reduced to oxidized impactor) have some effect on the heat content and temperature of the core.

Models of accretion where the depth of magma ocean is high will tend to favor hotter cores: for instance the models of Rubie et al. (2015) yields maximum pressure of equi-

libration between 72 and 80% of the CMB pressure would give higher CMB temperatures than models where the maximum pressure is set at 66% of the CMB pressure as in Fischer et al. (2015). Indeed, in the models of of (Rubie et al., 2015), the close equivalent parameter in our models would be $a_P \sim 0.72 - 0.8$, $f_c \simeq 0.93 - 0.99$ and $\lambda = 1$, which would yield $\overline{P_{eq}} = 45$ GPa and therefore $T^{is}_{CMB} > 4100$ K if we continue the trend of 8. In the case of Fischer et al. (2015), the closest equivalent parameter in our models would be $a_P = 0.66$, $f_c = 0.75$ and $\lambda = 1$, which yield $\overline{P_{eq}} = 38$ GPa, and an isentropic temperature at the CMB between 4000 and 4100 K. The comparison is easier in the latter case, because the chemical models are more similar.

A parameter controlling the heat content and temperature at the end of accretion, for a given composition range, is λ (parameter defining the sharpness of the transition from shallow to deep magma ocean). Increasing the value of this parameter leads to a decrease in temperature, for every case studied here (Figure 8) This means that models of accretion for which a deep magma ocean exists all along the accretion's process (e.g. Wood et al., 2008; Boujibar et al., 2014; Fischer et al., 2015; Rubie et al., 2015; Clesi et al., 2016) are favoring relatively high $T^{\mathrm{is}}_{\mathrm{CMB}}$, between 4000 and 4150 K after mixing, depending on the value of λ and ε. The temperature becomes higher if heat transfer to the mantle is a minor process (i.e. large diapir leading to large values of Pe number), and compression of the metal and gravitational dissipation ($\varepsilon > 0.1$) are the main processes controlling the core temperature.

On the other hand, models with large impacts at the end of accretion (e.g. Canup, 2004; Raymond et al., 2009; Grewal et al., 2019) leading to a rapid increase of magma ocean depth after a long period of shallow magma ocean ($\lambda \sim 3 - 5$ in our models), will favor lower core temperatures. This is because the adiabatic path followed by the metal is less steep than the liquidus of silicate (Figures 3, 4 and 8). Therefore the compression of the metallic diapir and the metallic core is not enough to compensate for the initial lower temperature of the metal during the shallow magma ocean stage. However, this effect can be erase if relatively high amounts of gravitational dissipation energy are transferred in the metal: as shown in Figure 9, the trend in temperature evolution shown in Figure 8 (Bottom row) is reversed for $\varepsilon > 0.05$. Therefore, models that propose core/mantle segregation in a shallow magma ocean followed by large impacts need to incorporate at least 5% of gravitational dissipation energy to produce core as hot as models that have a deep magma ocean all along the accretion.

If compression and dissipation are the main process controlling the temperature, this type of scenarios leads to $T^{\text{is}}_{\text{CMB}} \sim 3950$ K for compression only, and higher temperatures if $\varepsilon \neq 0$, up to 6500 K for $\varepsilon = 0.25$ and more probably $\leq$ 5000K for $\varepsilon < 0.1$.

Overall, the CMB temperature of the core, even after mixing, are in the lower end of the proposed temperature of the core obtained from different authors (King & Olson, 2011; Labrosse, 2015), and closer, but still higher, to the one determined by the solidus of pyrolite (Nomura et al., 2014). While adding a dissipation terms during the core formation does increases the temperature by 15%, it is still not enough to account for the relatively high temperatures proposed by several authors (up to 7000 K for King & Olson, 2011; Labrosse, 2015). One explanation may lie in the energy required to mix the core, which can change the overall heat budget of the core (Section 7.5.2).

7.3.3 Effect of Heat producing elements

As stated in Section 6.4, the temperature yielded by our models without any dissipation energy incorporation into the core ranges from 3925 K to 4150 K. The lowest values are close to the current estimates of CMB temperature (Nomura et al., 2014). One would expect, because of secular cooling, higher temperatures at the CMB in the early Earth than the temperature of today's CMB.

Our calculations ignore the possible effect of radioactive heating, and we estimate here the contribution of heat producing element (HPE) to the heat content of the core at the end of its formation. The main element producing heat in the core is K (Corgne et al., 2007; M. A. Bouhifd et al., 2007; Watanabe et al., 2014). U and Th concentrations in the core are low ($\sim$1.2 ppb and $\sim$ 5 ppb for U and Th, respectively, according to Faure et al., 2020) due to their lithophile behavior, and combined with long half-life, their contribution to the heat content of the early core is negligible.

The range of K concentration depends on the O concentration of the core (Corgne et al., 2007; M. A. Bouhifd et al., 2007; Watanabe et al., 2014; Faure et al., 2020), ranging from <1 ppm to $\sim$ 80 ppm for 0% wt and 9 % wt of O in the core, respectively. Our models yield low O concentrations ($\sim$ 2 %wt), which translates in a K concentration around 40 ppm. Using 40 ppm of K in the core, the heat production rate of 1.917×10^{-5} W.kg^{-1} from Weast et al. (1988), the present-day proportion of ^{40}K in total K of 0.0117% from

836 De Laeter et al. (2003), which translates in a proportion of 0.14% during core formation
837 4.56 Gy ago (using a decay constant $\lambda_{^{40}\mathrm{K}} = 0.55$ Gy^{-1}), and a timescale of core for-
838 mation between 30 and 100 millions years (Kleine et al., 2009), the supplementary heat
839 content due to ^{40}K decay ranges from $\sim 2.0 \times 10^{27}$ J to $\sim 6.7 \times 10^{27}$ J.

840 Even with 80 ppm of K in the core (highest estimate from Corgne et al., 2007), we
841 would get for a core forming in 100 millions years an additional $1.3{\times}10^{28}$ J, ~ 100 times
842 less than the heat content of the core we have estimated.

843 Therefore the assumption that we can neglect the heat producing elements in es-
844 timating the temperature of the early core is valid; adding K, U and Th into the chem-
845 ical model would not yield significantly different results.

846 After core formation, radioactive heating could only induce an increase of the core
847 temperature if the radioactive heat production exceeds the heat flux at the CMB. This
848 seems unlikely since the radioactive heat production in the core is likely modest even 4.56
849 Gy ago (around 2 TW with 40 ppm of K in the core, about 12 times higher than it is
850 today). Radioactive heating is therefore unlikely to help reconcile models yielding low
851 core temperatures with its present-day estimate.

852 ### 7.4 Using early core temperature as a constraining parameter for core
853 composition

854 With the simplifying hypothesis described in Section 4 and no dissipative heating
855 in the metal, the predictions of T^{is}_{CMB} obtained with our model are all in the same range
856 as the estimates of the current CMB temperature. Some of the geochemically consistent
857 scenarios yield CMB temperatures that are lower than the current estimates. This can
858 be interpretated in different ways:

859 i) The equation of state of liquid metal (Equation 29) and the value of Grüneisen
860 parameter (Equation 31) are poorly chosen and leads to an underestimation of the
861 metal temperature during compression. As discussed in section 7.1, the core tem-
862 perature is indeed quite sensitive to the choice of equation of state formalism and
863 parameters.
864 ii) Giant impacts that do not equilibrate with the magma ocean (core-merging pro-
865 cess) can lead to higher temperature of the metal accreting to the core at the end

of the core formation (Canup, 2004; Suer et al., 2021). Since our model does not take this hypothesis into account, the temperatures predicted by the model may be underestimated.

iii) The radioactive heat production within the core is larger than the heat flux at the CMB for some time after core formation, resulting in an increase of the temperature of the core. This is however highy unlikely, as discussed in Section 7.3.3.

iv) All of the previous hypothesis have been taken into account (strong confidence in equation of state, giant impacts and incorporation of heat producing elements) and the temperature is still lower than the current CMB temperature. In such a case, despite the model being consistent chemically, it is not thermally consistent and therefore can be discarded

If interpretation iv) can be used for our model or any other similar model of core-mantle segregation, then it is possible to discard core-formation scenarios and core compositions on the basis of the core temperature, despite the composition being chemically accurate in regards to the BSE. Core temperature could then become one more parameter used to constrain the core composition and core-formation processes, thanks to the positive correlation predicted by the model between light elements concentration, core temperature, and mean equilibration pressure (Figure 8).

7.5 Core composition and primordial chemical stratification

In this section we propose some interpretations on how we can accrete a stratified core (Jacobson et al., 2017) into a well mixed core and the potential energy variation associated with it.

7.5.1 Compositional stratification of the core

Our results yield a range of bulk compositions for the core that are in agreement with previous studies: $\sim$ 90% of Fe-Ni alloy combined with $\sim$ 10 % of light elements, in our case Si and O (Figure 5, bottom panels). Since the core formed in several steps, it can end up being chemically and thermally stratified, depending on the degree of mixing which may follow the formation of the core (Jacobson et al., 2017; Landeau et al., 2017).

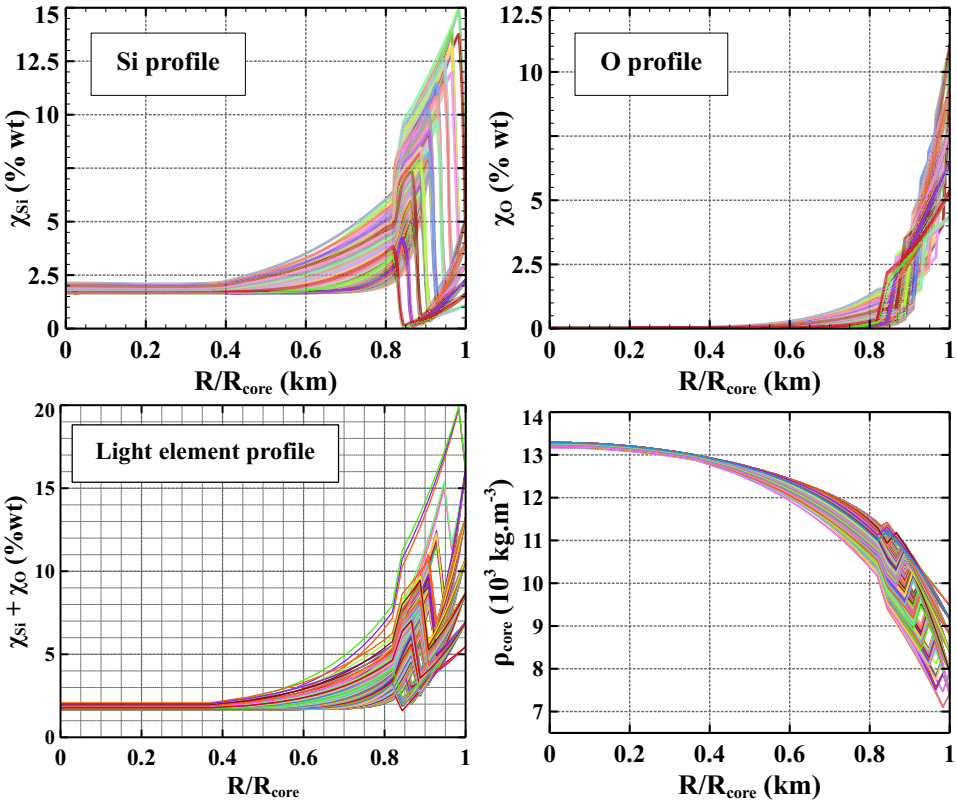

Figure 10. Evolution of the light element content in the core for all the solutions of our model as a function of normalized core radius ($R_{core} = 3470km$). Top left: χ_{Si} (% wt). Top right: χ_O (% wt). Bottom left: $\chi_{Si} + \chi_O$. Bottom right: $\rho_{core}(10^3 \text{kg.m}^{-3})$. Each line is a solution of the model corresponding to the bulk composition shown in Figure 5.

Figure 10 shows that the bulk compositions we obtain cover a large range of possible stratifications. Locally, the sum of Si and O concentrations can be up to 20% wt (bottom panel, Figure 10), while the overall bulk core concentration is still less than 10% wt (Figure 5, bottom panels). Another feature of the stratified model is that the center of the core is less rich in light elements, due to a lower pressure of equilibration and thus a lower value for K_d for both element. The concentration in light element increases toward the CMB, since the metal close to the CMB equilibrated with silicates at higher pressures. The main light element is silicon, which gets incorporated earlier in the accretion history. Oxygen becomes a more prominent element at the end of accretion, for more oxidizing impactors; its concentration is therefore high only in the upper part of the core. The concentration of Si drops once the condition of accretion are more oxidizing, leading to more oxygen being incorporated in the core. This behaviour is expected since Si and O tend to exclude each other in the metallic melt (Frost et al., 2010; Ricolleau et al., 2011). The stratification is therefore not smooth, and can be non-monotonic: though the concentration profile is stably stratified in most of the core, there is often a region where it is unstably stratified (concentration of light elements increasing with depth). The concentration in light elements often reaches its maximum a few hundred kilometers below the CMB (R $\sim$ 2500-3000 km).

The chemical stratification could be conserved in the current core (Bouffard et al., 2020; Landeau et al., 2021), but for the rest of the paper we will focus on the implications of going from a stratified core as given by our models to a fully mixed core for which we calculated the isentropic temperature.

7.5.2 Variations of potential energy and implications for core mixing processes

Going from a stratified profile to a mixed profile changes the potential energy of the core, which is

$$E_p = 4\pi \int_0^{R_{\rm CMB}} g(r)\rho(r)r^3 dr \tag{38}$$

(Birch, 1965; Flasar & Birch, 1973), where $g(r)$ is the gravitational field in the core given by interpolation of the density profile and integration of the Gauss theorem for gravitation. The total potential energy for both model (stratified and mixed) is shown in Figure S8 and S9, and ranges from $\sim$ 3.8 to 4.7 10^{31} J for both profiles. The variation of

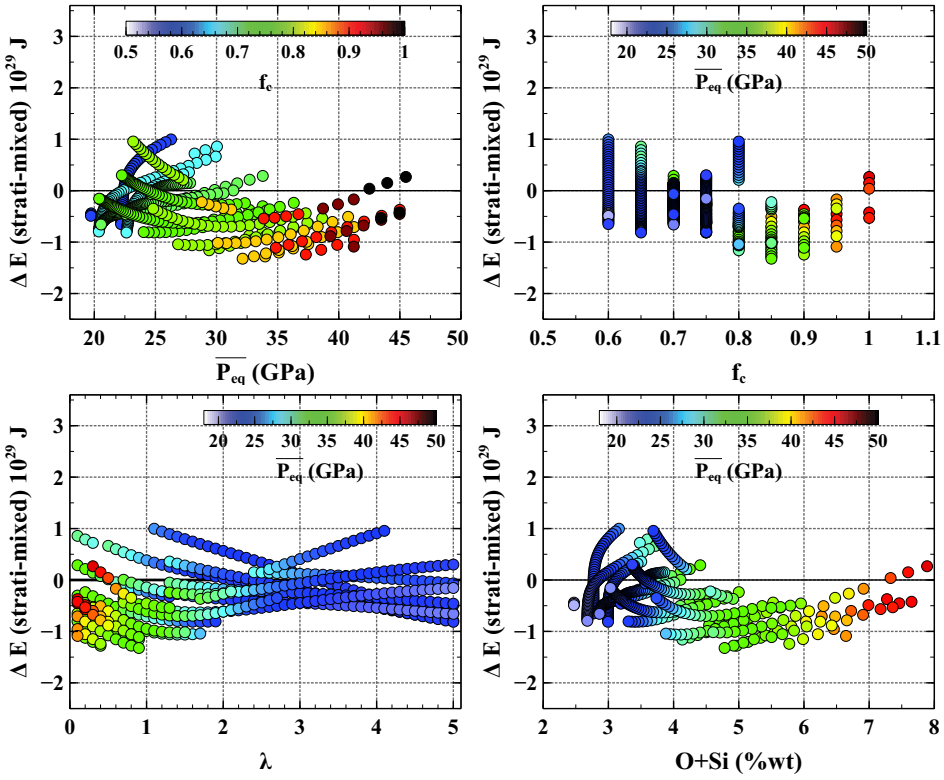

Figure 11. $\Delta E = E_p^{\text{strati}} - E_p^{\text{mixed}}$ calculated from Equation 38 for the density profiles obtained at the end of accretion (E_p^{strati}, Figure 10) and after core mixing (E_p^{mixed}), as a function of $\overline{P_{eq}}$, f_c, λ and χ_{Si+O}. The black line separate negative value from positive value. The physical and chemical meaning of the parameters is explained in Section 3.1.2 and in Table 2.

potential energy between the stratified and mixed situations is calculated as $\Delta E = E_p^{\text{strati}} - E_p^{\text{mixed}}$. If $\Delta E < 0$, then the potential energy of the mixed profile is higher than the potential energy of the initial stratified profile, which means that mixing the core would require an energy input. If $\Delta E > 0$, then mixing the core would lead to a release of energy, and would therefore be energetically favored.

Figure 11 shows that the variation in potential energy is between -1.32 x 10^{29} J and 0.96 x 10^{29} J, corresponding to $\sim \pm 1$ % of the total potential energy of the core (Figure S8 and S9). Most of our models (76%) yield $\Delta E < 0$, but a significant number (24 %, 117 models) of solutions yield $\Delta E > 0$. One could have expected ΔE to be always negative, corresponding to monotonically stably stratified profiles, but as shown on Figure 10, the concentration profile, though stably stratified in most of the core, is often unstably stratified in a region a few hundred kilometers below the CMB. ΔE can be either

negative or positive depending on the relative importance of the stably and unstably stratified regions.

Figure 11 shows no clear trend between ΔE and the values of $\overline{P_{eq}}$, f_c (parameter defining both the moment in accretion when P_{eq} increase faster at high λ values and the transition from reduced to oxidized impactor), λ (parameter defining the sharpness of the transition from shallow to deep magma ocean) or the light element concentrations. As shown in Section 7.5.1, the uppermost 20 to 30% of the core (2500- 3470 km) is where the variations in light element concentrations are the most important. Since it is also where $g(r)$ is the highest, this region is the controlling factor of the potential energy change. In 25% of the case, the combination of light element concentration changes with the gravitational field can create a high enough gravitational instability in the core to yield positive ΔE. It shows that incorporation of oxygen in the core, proposed by several authors (Frost et al., 2010; Ricolleau et al., 2011; Fischer et al., 2015) can facilitate to some extent the mixing of the core, and participate, at least to some extent, to the destruction of a core stratification (Landeau et al., 2016; Bouffard et al., 2020).

When $\Delta E > 0$, partial or complete mixing of the core may still arise due to external mechanical forcing resulting from giant impacts. The energy release by a giant impact, as estimated by Lock et al. (2020) or Carter et al. (2020), may be in the range of 10^{31} to 10^{32} J, much larger than the $\sim 10^{29}$ J energy variation needed to mix the core. The fraction of this energy available to mix the core is difficult to estimate, as recognized by Jacobson et al. (2017) and (Bouffard et al., 2020), but we note that mixing the core necessitates only a few % of the kinetic energy release by a Moon-forming giant impact. This is consistent with the Jacobson et al. (2017) model, which takes a fraction of 4% from the initial impactor energy release, as well as Bouffard et al. (2020) who proposed an energy transfer to the core corresponding to 0.5 to 1% of the impactor energy release. These amount are kinetic energy are an upper bound, since it possible to mix some of the core everytime some metal reaches the core (Landeau et al., 2016).

8 Conclusion

In this study we build a parameterized model of accretion linking the core temperature with the composition of the mantle. The model successfully proves that it is possible to link the core temperature at the end of accretion to the core composition, provided a certain number of parameters are sufficiently known (Equations of state, silicate

liquidus, partitioning behaviour). To obtain a composition close to the Earth, it is necessary to accrete 60 to 80 % of reduced material, and to equilibrate metal and silicate in a magma ocean at an average pressure between 20 and 45 GPa (the average being taken on the full accretion process). The temperature of the core is higher if the magma ocean is maintained throughout the entire accretion, while a transition from a shallow to a deep magma ocean favor lower temperature of the core. The heat content and temperature of the core are controlled by the compressional heating during metallic descent, with negligible effect of diffusion between the diapirs and surrounding mantle, and small effect of the dissipation of gravitational energy. The initial heat content, ranging from 8.92 to 9.55 10^{30} J, is dependent on the evolution of the metal-silicate segregation.

Our models favor relatively 'cold' mixed core, with the more probable range of CMB temperature (after core mixing) between $\sim$ 3950 and 4150 K, depending on the accretion style. Loss of heat to the mantle is a negligible phenomena affecting the core temperature compared to the compressional heating. Dissipation of gravitational energy may increase strongly the temperature, for example up to 6500 K if 25% of the gravitational energy released during core formation is dissipated in the metal.

For most of the accretion scenarios, mixing the core from a stratified state to a homogeneous and isentropic state requires an external source of energy which represent only a few percent of the kinetic energy of an impact (10^{29} J of potential energy change compared to 10^{31} to 10^{32} J for the kinetic energy delivered by giant impacts). It is possible in some case that no external energy is needed: in some scenarios at least parts of the core are unstably stratified, which will facilitate the mixing of the core. On the other hand, models where there is dramatic increasing of the depth at the end of accretion yield more stable stratifications, and therefore other sources of energy need to be added to the core to account for mixing the core.

Further modeling is necessary to improve the chemical model on the partitioning of chalcophile elements and heat producing elements so as to further constrain the initial thermal conditions.

It will in principle be possible to constrain the core composition by using the temperature of the core as well as the density. This goal can be achieved by constraining further the parameters we used (such as the formation of a basal magma ocean, partition-

998 ing of the heat producing elements into the core, adequate equation of state of liquide
999 metal), by experimental work or *ab initio* calculation.

1000 Acknowledgments

1001 This work was supported by the European Research Council (ERC) under the Eu-
1002 ropean Unions Horizon 2020 research and innovation programme (grant number 716429).
1003 ISTerre is part of Labex OSUG@2020 (ANR10 LABX56). The authors declare no other
1004 sources of funding and no competing interest. The authors are very greatful to Maxime
1005 Maurice and Guillaume Morard for their fruitful comments. The authors thanks Car-
1006 olina Lithgow-Bertelloni for the editorial handling of the paper and two anonymous re-
1007 viewers for their comments.

1008 Availability of the data

1009 The code used in this study, as well as a simplified version, can be downloaded on
1010 the Zenodo repository following this link: `https://doi.org/10.5281/zenodo.7661374`.

1011 References

1012 Alfè, D., Price, G., & Gillan, M. (2002). Iron under Earth's core conditions: Liquid-
1013 state thermodynamics and high-pressure melting curve from ab initio calcula-
1014 tions. *Physical Review B*, *65*(16), 165118.

1015 Al'Tshuler, L., Brusnikin, S., & Kuz'Menkov, E. (1987). Isotherms and Grüneisen
1016 functions for 25 metals. *Journal of Applied Mechanics and Technical Physics*,
1017 *28*(1), 129–141.

1018 Anderson, W. W., & Ahrens, T. J. (1994). An equation of state for liquid iron
1019 and implications for the Earth's core. *Journal of Geophysical Research: Solid*
1020 *Earth*, *99*(B3), 4273–4284.

1021 Andrault, D., Bolfan-Casanova, N., Nigro, G. L., Bouhifd, M. A., Garbarino, G., &
1022 Mezouar, M. (2011). Solidus and liquidus profiles of chondritic mantle: Impli-
1023 cation for melting of the Earth across its history. *Earth and planetary science*
1024 *letters*, *304*(1-2), 251–259.

1025 Andrault, D., Monteux, J., Le Bars, M., & Samuel, H. (2016). The deep Earth may
1026 not be cooling down. *Earth and planetary science letters*, *443*, 195–203.

1027 Armstrong, K., Frost, D. J., McCammon, C. A., Rubie, D. C., & Ballaran, T. B.

(2019). Deep magma ocean formation set the oxidation state of Earth's mantle. *Science*, *365*(6456), 903–906.

Badro, J., Aubert, J., Hirose, K., Nomura, R., Blanchard, I., Borensztajn, S., & Siebert, J. (2018). Magnesium partitioning between Earth's mantle and core and its potential to drive an early exsolution geodynamo. *Geophysical Research Letters*, *45*(24), 13–240.

Badro, J., Brodholt, J. P., Piet, H., Siebert, J., & Ryerson, F. J. (2015). Core formation and core composition from coupled geochemical and geophysical constraints. *Proceedings of the National Academy of Sciences*, *112*(40), 12310–12314.

Batchelor, G. K. (1967). *An Introduction to Fluid Dynamics* (Batchelor, G. K., Ed.).

Birch, F. (1964). Density and composition of mantle and core. *Journal of geophysical research*, *69*(20), 4377–4388.

Birch, F. (1965). Energetics of core formation. *Journal of Geophysical research*, *70*(24), 6217–6221.

Bouffard, M., Landeau, M., & Goument, A. (2020). Convective erosion of a primordial stratification atop Earth's core. *Geophysical Research Letters*, *47*(14), e2020GL087109.

Bouhifd, M., & Jephcoat, A. (2011, July). Convergence of Ni and Co metal–silicate partition coefficients in the deep magma-ocean and coupled silicon–oxygen solubility in iron melts at high pressures. *Earth and Planetary Science Letters*, *307*(3-4), 341–348.

Bouhifd, M. A., Gautron, L., Bolfan-Casanova, N., Malavergne, V., Hammouda, T., Andrault, D., & Jephcoat, A. (2007). Potassium partitioning into molten iron alloys at high-pressure: Implications for Earth's core. *Physics of the Earth and Planetary Interiors*, *160*(1), 22–33.

Bouhifd, M. A., & Jephcoat, A. P. (2003). The effect of pressure on partitioning of Ni and Co between silicate and iron-rich metal liquids: a diamond-anvil cell study. *Earth and planetary science letters*, *209*(1-2), 245–255.

Boujibar, A., Andrault, D., Bouhifd, M., Bolfan-Casanova, N., Devidal, J.-L., & Trcera, N. (2014, April). Metal–silicate partitioning of sulphur, new experimental and thermodynamic constraints on planetary accretion. *Earth and*

Planetary Science Letters, *391*, 42–54.

Canup, R. M. (2004). Simulations of a late lunar-forming impact. *Icarus*, *168*(2), 433–456.

Carter, P. J., Lock, S. J., & Stewart, S. T. (2020). The energy budgets of giant impacts. *Journal of Geophysical Research: Planets*, *125*(1), e2019JE006042.

Cartier, C., Hammouda, T., Boyet, M., Bouhifd, M. A., & Devidal, J.-L. (2014). Redox control of the fractionation of niobium and tantalum during planetary accretion and core formation. *Nature Geoscience*, *7*(8), 573–576.

Cartier, C., Hammouda, T., Doucelance, R., Boyet, M., Devidal, J.-L., & Moine, B. (2014). Experimental study of trace element partitioning between enstatite and melt in enstatite chondrites at low oxygen fugacities and 5 GPa. *Geochimica et Cosmochimica Acta*, *130*, 167–187.

Chi, H., Dasgupta, R., Duncan, M. S., & Shimizu, N. (2014). Partitioning of carbon between Fe-rich alloy melt and silicate melt in a magma ocean–implications for the abundance and origin of volatiles in Earth, Mars, and the Moon. *Geochimica et Cosmochimica Acta*, *139*, 447–471.

Clesi, V., Bouhifd, M., Bolfan-Casanova, N., Manthilake, G., Fabbrizio, A., & Andrault, D. (2016). Effect of H2O on metal–silicate partitioning of Ni, Co, V, Cr, Mn and Fe: Implications for the oxidation state of the Earth and Mars. *Geochimica et Cosmochimica Acta*, *192*, 97–121.

Clesi, V., Bouhifd, M. A., Bolfan-Casanova, N., Manthilake, G., Schiavi, F., Raepsaet, C., ... Andrault, D. (2018). Low hydrogen contents in the cores of terrestrial planets. *Science advances*, *4*(3), e1701876.

Clesi, V., Monteux, J., Qaddah, B., Le Bars, M., Wacheul, J.-B., & Bouhifd, M. A. (2020). Dynamics of core-mantle separation: Influence of viscosity contrast and metal/silicate partition coefficients on the chemical equilibrium. *Physics of the Earth and Planetary Interiors*, *306*, 106547.

Corgne, A., Keshav, S., Fei, Y., & McDonough, W. F. (2007). How much potassium is in the earth's core? new insights from partitioning experiments. *Earth and Planetary Science Letters*, *256*(3-4), 567–576.

Dasgupta, R., & Grewal, D. S. (2019). Origin and early differentiation of carbon and associated life-essential volatile elements on Earth. *Deep Carbon*, 4–39.

Deguen, R., & Cardin, P. (2011). Thermochemical convection in Earth's inner core.

Geophysical Journal International, *187*(3), 1101–1118.

de Koker, N., Steinle-Neumann, G., & Vlček, V. (2012). Electrical resistivity and thermal conductivity of liquid Fe alloys at high P and T, and heat flux in Earth's core. *Proceedings of the National Academy of Sciences*, *109*(11), 4070–4073.

De Laeter, J. R., Böhlke, J. K., De Bievre, P., Hidaka, H., Peiser, H., Rosman, K., & Taylor, P. (2003). Atomic weights of the elements. review 2000 (iupac technical report). *Pure and applied chemistry*, *75*(6), 683–800.

Dewaele, A., Loubeyre, P., Occelli, F., Mezouar, M., Dorogokupets, P. I., & Torrent, M. (2006). Quasihydrostatic equation of state of iron above 2 Mbar. *Physical Review Letters*, *97*(21), 215504.

Dorogokupets, P., Dymshits, A., Litasov, K., & Sokolova, T. (2017). Thermodynamics and Equations of State of Iron to 350 GPa and 6000 K. *Scientific reports*, *7*(1), 1–11.

Drake, M. J., & Righter, K. (2002). Determining the composition of the Earth. *Nature*, *416*(6876), 39–44.

Dubrovinsky, L., Saxena, S., Dubrovinskaia, N., Rekhi, S., & Le Bihan, T. (2000). Gruneisen parameter of ε-iron up to 300 GPa from in-situ X-ray study. *American Mineralogist*, *85*(2), 386–389.

Dziewonski, A. M., & Anderson, D. L. (1981). Preliminary reference Earth model. *Physics of the earth and planetary interiors*, *25*(4), 297–356.

Faure, P., Bouhifd, M. A., Boyet, M., Manthilake, G., Clesi, V., & Devidal, J.-L. (2020). Uranium and thorium partitioning in the bulk silicate Earth and the oxygen content of Earth's core. *Geochimica et Cosmochimica Acta*, *275*, 83–98.

Fischer, R. A., Nakajima, Y., Campbell, A. J., Frost, D. J., Harries, D., Langenhorst, F., ... Rubie, D. C. (2015). High pressure metal–silicate partitioning of Ni, Co, V, Cr, Si, and O. *Geochimica et Cosmochimica Acta*, *167*, 177–194.

Flasar, F. M., & Birch, F. (1973). Energetics of core formation: a correction. *Journal of Geophysical Research*, *78*(26), 6101–6103.

Fleck, J., Rains, C., Weeraratne, D., Nguyen, C., Brand, D., Klein, S., ... Olson, P. (2018). Iron diapirs entrain silicates to the core and initiate thermochemical plumes. *Nature communications*, *9*(1), 1–12.

Frost, D. J., Asahara, Y., Rubie, D. C., Miyajima, N., Dubrovinsky, L. S., Holzapfel, C., ... Sakai, T. (2010). Partitioning of oxygen between the Earth's mantle and core. *Journal of Geophysical Research: Solid Earth*, *115*(B2).

Grewal, D. S., Dasgupta, R., Sun, C., Tsuno, K., & Costin, G. (2019). Delivery of carbon, nitrogen, and sulfur to the silicate Earth by a giant impact. *Science advances*, *5*(1), eaau3669.

Hirose, K., Labrosse, S., & Hernlund, J. (2013). Composition and state of the core. *Annual Review of Earth and Planetary Sciences*, *41*, 657–691.

Ichikawa, H., Tsuchiya, T., & Tange, Y. (2014). The p-v-t equation of state and thermodynamic properties of liquid iron. *Journal of Geophysical Research: Solid Earth*, *119*(1), 240–252.

Irving, J. C., Cottaar, S., & Lekić, V. (2018). Seismically determined elastic parameters for Earth's outer core. *Science advances*, *4*(6), eaar2538.

Izidoro, A., Bitsch, B., & Dasgupta, R. (2021). The effect of a strong pressure bump in the Sun's natal disk: terrestrial planet formation via planetesimal accretion rather than pebble accretion. *The Astrophysical Journal*, *915*(1), 62.

Jacobson, S. A., Rubie, D. C., Hernlund, J., Morbidelli, A., & Nakajima, M. (2017). Formation, stratification, and mixing of the cores of Earth and Venus. *Earth and Planetary Science Letters*, *474*, 375–386.

Ke, Y., & Solomatov, V. (2009). Coupled core-mantle thermal evolution of early Mars. *Journal of Geophysical Research: Planets*, *114*(E7).

King, C., & Olson, P. (2011). Heat partitioning in metal-silicate plumes during Earth differentiation. *Earth and Planetary Science Letters*, *304*(3-4), 577–586.

Kleine, T., Touboul, M., Bourdon, B., Nimmo, F., Mezger, K., Palme, H., ... Halliday, A. N. (2009). Hf–W chronology of the accretion and early evolution of asteroids and terrestrial planets. *Geochimica et Cosmochimica Acta*, *73*(17), 5150–5188.

Kono, Y., Kenney-Benson, C., Shibazaki, Y., Park, C., Shen, G., & Wang, Y. (2015, April). High-pressure viscosity of liquid Fe and FeS revisited by falling sphere viscometry using ultrafast X-ray imaging. *Physics of the Earth and Planetary Interiors*, *241*, 57–64. Retrieved 2023-01-25, from `https://www.sciencedirect.com/science/article/pii/S0031920115000229` doi: 10.1016/j.pepi.2015.02.006

Kuwayama, Y., Morard, G., Nakajima, Y., Hirose, K., Baron, A. Q., Kawaguchi, S. I., ... Ohishi, Y. (2020). Equation of state of liquid iron under extreme conditions. *Physical Review Letters*, *124*(16), 165701.

Labrosse, S. (2015). Thermal evolution of the core with a high thermal conductivity. *Physics of the Earth and Planetary Interiors*, *247*, 36–55.

Landeau, M., Aubert, J., & Olson, P. (2017). The signature of inner-core nucleation on the geodynamo. *Earth and Planetary Science Letters*, *465*, 193–204.

Landeau, M., Deguen, R., Phillips, D., Neufeld, J. A., Lherm, V., & Dalziel, S. B. (2021). Metal-silicate mixing by large Earth-forming impacts. *Earth and Planetary Science Letters*, *564*, 116888.

Landeau, M., Olson, P., Deguen, R., & Hirsh, B. H. (2016). Core merging and stratification following giant impact. *Nature Geoscience*, *9*(10), 786–789.

Laurenz, V., Rubie, D. C., Frost, D. J., & Vogel, A. K. (2016). The importance of sulfur for the behavior of highly-siderophile elements during Earth's differentiation. *Geochimica et Cosmochimica Acta*, *194*, 123–138.

Lock, S. J., Stewart, S. T., & Ćuk, M. (2020). The energy budget and figure of Earth during recovery from the Moon-forming giant impact. *Earth and Planetary Science Letters*, *530*, 115885.

Malavergne, V., Bureau, H., Raepsaet, C., Gaillard, F., Poncet, M., Surble, S., ... others (2019). Experimental constraints on the fate of H and C during planetary core-mantle differentiation. Implications for the Earth. *Icarus*, *321*, 473–485.

McDonough, W. (2003). Compositional model for the earth core. *Treatise on geochemistry*, 547–568.

McDonough, W., & Sun, S.-S. (1995). The composition of the Earth. *Chemical geology*, *120*(3-4), 223–253.

Monteux, J., Ricard, Y., Coltice, N., Dubuffet, F., & Ulvrova, M. (2009). A model of metal–silicate separation on growing planets. *Earth and Planetary Science Letters*, *287*(3-4), 353–362.

Morard, G., Siebert, J., Andrault, D., Guignot, N., Garbarino, G., Guyot, F., & Antonangeli, D. (2013). The Earth's core composition from high pressure density measurements of liquid iron alloys. *Earth and Planetary Science Letters*, *373*, 169–178.

1193 Morbidelli, A., Chambers, J., Lunine, J., Petit, J.-M., Robert, F., Valsecchi, G., &
1194 Cyr, K. (2000). Source regions and timescales for the delivery of water to the
1195 Earth. *Meteoritics & Planetary Science*, *35*(6), 1309–1320.
1196 Morris, S. (1982). The effects of a strongly temperature-dependent viscosity on slow
1197 flow past a hot sphere. *J. Fluid Mech.*, *124*, 1-26.
1198 Murnaghan, F. D. (1944). The compressibility of media under extreme pressures.
1199 *Proceedings of the National Academy of Sciences*, *30*(9), 244–247.
1200 Nakajima, M., Golabek, G. J., Wünnemann, K., Rubie, D. C., Burger, C., Melosh,
1201 H. J., ... Hull, S. D. (2021). Scaling laws for the geometry of an impact-
1202 induced magma ocean. *Earth and Planetary Science Letters*, *568*, 116983.
1203 Nimmo, F. (2007). Energetics of the core. *Treatise on geophysics*, *8*, 31–65.
1204 Nimmo, F., & Kleine, T. (2015). Early differentiation and core formation: processes
1205 and timescales. *The early Earth: accretion and differentiation*, 83–102.
1206 Nomura, R., Hirose, K., Uesugi, K., Ohishi, Y., Tsuchiyama, A., Miyake, A., &
1207 Ueno, Y. (2014). Low core-mantle boundary temperature inferred from the
1208 solidus of pyrolite. *Science*, *343*(6170), 522–525.
1209 Olson, P., & Weeraratne, D. (2008). Experiments on metal–silicate plumes and core
1210 formation. *Philosophical Transactions of the Royal Society A: Mathematical,*
1211 *Physical and Engineering Sciences*, *366*(1883), 4253–4271.
1212 O'Brien, D. P., Walsh, K. J., Morbidelli, A., Raymond, S. N., & Mandell, A. M.
1213 (2014). Water delivery and giant impacts in the 'Grand Tack'scenario. *Icarus*,
1214 *239*, 74–84.
1215 Raymond, S. N., & Izidoro, A. (2017). Origin of water in the inner solar system:
1216 Planetesimals scattered inward during jupiter and saturn's rapid gas accretion.
1217 *Icarus*, *297*, 134–148.
1218 Raymond, S. N., O'Brien, D. P., Morbidelli, A., & Kaib, N. A. (2009). Building the
1219 terrestrial planets: Constrained accretion in the inner Solar System. *Icarus*,
1220 *203*(2), 644–662.
1221 Ribe, N. (1983). Diapirism in the earth's mantle: experiments on the motion of
1222 a hot sphere in a fluid with temperature dependent viscosity. *Journal of Vol-*
1223 *canology and Geothermal Research*, *16*, 221-245.
1224 Ricolleau, A., Fei, Y., Corgne, A., Siebert, J., & Badro, J. (2011). Oxygen and
1225 silicon contents of Earth's core from high pressure metal–silicate partitioning

experiments. *Earth and Planetary Science Letters*, *310*(3-4), 409–421.

Righter, K. (2011, April). Prediction of metal–silicate partition coefficients for siderophile elements: An update and assessment of P-T conditions for metal–silicate equilibrium during accretion of the Earth. *Earth and Planetary Science Letters*, *304*(1-2), 158–167.

Roskosz, M., Bouhifd, M. A., Jephcoat, A., Marty, B., & Mysen, B. (2013). Nitrogen solubility in molten metal and silicate at high pressure and temperature. *Geochimica et Cosmochimica Acta*, *121*, 15–28.

Rubie, D., Frost, D., Mann, U., Asahara, Y., Nimmo, F., Tsuno, K., ... Palme, H. (2011). Heterogeneous accretion, composition and core–mantle differentiation of the Earth. *Earth and Planetary Science Letters*, *301*(1-2), 31–42.

Rubie, D., Jacobson, S., Morbidelli, A., O'Brien, D., Young, E., de Vries, J., ... Frost, D. (2015, March). Accretion and differentiation of the terrestrial planets with implications for the compositions of early-formed Solar System bodies and accretion of water. *Icarus*, *248*, 89–108.

Rubie, D., Melosh, H., Reid, J., Liebske, C., & Righter, K. (2003). Mechanisms of metal–silicate equilibration in the terrestrial magma ocean. *Earth and Planetary Science Letters*, *205*(3-4), 239–255.

Samuel, H., Tackley, P., & Evonuk, M. (2010). Heat partitioning in terrestrial planets during core formation by negative diapirism. *Earth and Planetary Science Letters*, *290*(1-2), 13–19.

Sanloup, C., Guyot, F., Gillet, P., Fiquet, G., Mezouar, M., & Martinez, I. (2000). Density measurements of liquid Fe-S alloys at high-pressure. *Geophysical Research Letters*, *27*(6), 811–814.

Seagle, C. T., Cottrell, E., Fei, Y., Hummer, D. R., & Prakapenka, V. B. (2013). Electrical and thermal transport properties of iron and iron-silicon alloy at high pressure. *Geophysical Research Letters*, *40*(20), 5377–5381.

Siebert, J., Badro, J., Antonangeli, D., & Ryerson, F. J. (2012). Metal–silicate partitioning of Ni and Co in a deep magma ocean. *Earth and Planetary Science Letters*, *321*, 189–197.

Siebert, J., Badro, J., Antonangeli, D., & Ryerson, F. J. (2013). Terrestrial accretion under oxidizing conditions. *Science*, *339*(6124), 1194–1197.

Speelmanns, I. M., Schmidt, M. W., & Liebske, C. (2018). Nitrogen solubility in

core materials. *Geophysical Research Letters*, *45*(15), 7434–7443.

Suer, T.-A., Siebert, J., Remusat, L., Day, J. M., Borensztajn, S., Doisneau, B., & Fiquet, G. (2021). Reconciling metal–silicate partitioning and late accretion in the earth. *Nature Communications*, *12*(1), 2913.

Tennekes, H., & Lumley, J. L. (1972). *First Course in Turbulence*. MIT Press.

Tonks, W. B., & Melosh, H. J. (1993). Magma ocean formation due to giant impacts. *Journal of Geophysical Research: Planets*, *98*(E3), 5319–5333.

Tsuno, K., Frost, D. J., & Rubie, D. C. (2013). Simultaneous partitioning of silicon and oxygen into the Earth's core during early Earth differentiation. *Geophysical Research Letters*, *40*(1), 66–71.

Tuff, J., Wood, B., & Wade, J. (2011, January). The effect of Si on metal–silicate partitioning of siderophile elements and implications for the conditions of core formation. *Geochimica et Cosmochimica Acta*, *75*(2), 673–690.

Turcotte, D. L., & Schubert, G. (2002). *Geodynamics*. Cambridge university press.

Ulvrová, M., Coltice, N., Ricard, Y., Labrosse, S., Dubuffet, F., Velímskỳ, J., & Šrámek, O. (2011). Compositional and thermal equilibration of particles, drops and diapirs in geophysical flows. *Geochemistry Geophysics Geosystems*, *12*(10), 1–11.

Umemoto, K., Hirose, K., Imada, S., Nakajima, Y., Komabayashi, T., Tsutsui, S., & Baron, A. Q. (2014). Liquid iron-sulfur alloys at outer core conditions by first-principles calculations. *Geophysical Research Letters*, *41*(19), 6712–6717.

Wade, J., & Wood, B. (2005). Core formation and the oxidation state of the earth. *Earth and Planetary Science Letters*, *236*(1-2), 78–95.

Wasson, J. T., & Kallemeyn, G. W. (1988). Compositions of chondrites. *Philosophical Transactions of the Royal Society of London. Series A, Mathematical and Physical Sciences*, *325*(1587), 535–544.

Watanabe, K., Ohtani, E., Kamada, S., Sakamaki, T., Miyahara, M., & Ito, Y. (2014). The abundance of potassium in the earth's core. *Physics of the Earth and Planetary Interiors*, *237*, 65–72.

Weast, R. C., et al. (1988). *Handbook of chemistry and physics*. Springer.

Wood, B., Wade, J., & Kilburn, M. (2008, March). Core formation and the oxidation state of the Earth: Additional constraints from Nb, V and Cr partitioning. *Geochimica et Cosmochimica Acta*, *72*(5), 1415–1426.

Zhang, Y., Sekine, T., Lin, J.-F., He, H., Liu, F., Zhang, M., ... Yu, Y. (2018). Shock compression and melting of an Fe-Ni-Si alloy: Implications for the temperature profile of the Earth's core and the heat flux across the core-mantle boundary. *Journal of Geophysical Research: Solid Earth*, *123*(2), 1314–1327.

Supporting Information for "Linking the core heat content to Earth's accretion history"

Contents of this file

1. Text S1 to S4
2. Figures S1 to S9
3. Table S1

S1. Calculation of the thermal model

In this section we show the different steps of transformation necessary to go from Equation 1 :

$$\rho_m C_{p,m} \frac{dT}{dt} = -\nabla \cdot q + \rho_m C_{p,m} T \frac{\gamma}{K_{s,m}} \frac{dP}{dT} + \Phi, \tag{1}$$

to the solution used in our models Equation 2:

$$T(P) = \exp\left[-\int_{P_{eq}}^{P} A(P')dP'\right] \times \left[\int_{P_{eq}}^{P} B(P') \exp\left(-\int_{P_{eq}}^{P'} A(P'')dP''\right) dP' + constant\right] \tag{2}$$

When Equation 1 is integrated on the mass of metallic diapir (M_d for the radius R_d) we get $\rho_m C_{p,m} \frac{dT}{dt} = M_d c_{p,m} \frac{DT}{dt}$ for the left-hand side of the equation. Applying the integration on the right hand-side and making $\frac{DT}{dt}$ the only term on the left-hand side of the equation

we get:

$$\frac{dT}{dt} = \frac{-4\pi R_d k_s (T - T_{sm})}{c_{p,m} M_d} Nu + T \frac{\gamma}{K_{s,m}} \frac{dP}{dT} + M_d \frac{\Phi}{\rho_m c_{p,m}} \tag{3}$$

If we consider the gravitational field in the mantle to be constant for a given step of accretion, we can have the relation $\frac{dP}{dz} = -\rho_s g$. We can then introduce a time-depth-pressure relationship to express variations of temperature as a function of pressure in the accreting planet. The relationship is given by:

$$\frac{dT}{dt} = -v_d \frac{dT}{dz} = \rho_s g v_d \tag{4}$$

Combining Equations 3 and 4, as well as making a change in the first term in the right-hand side of Equation 3 to make ρ_m appear and simplifying the compression term, we get the following relationship:

$$\frac{dT}{dP} = -\frac{3}{R_d^2} \frac{k_s (T - T_{sm})}{\rho_m c_{p,m} \rho_s g v_d} Nu + T \frac{\gamma}{K_{s,m}} + \frac{\Phi}{\rho_m c_{p,m} \rho_s g v_d} \tag{5}$$

The total dissipation energy that can be dissipated in the metal is calculated by the relation $\phi_{tot} = \Delta\rho g v_d^2$, with $\Delta\rho = \rho_m - \rho_s$. The value of Φ is a fraction (ε) of the total dissipation energy that can heat the metal, given by the relation $\Phi = \varepsilon \phi_{tot} / v_d$. We therefore have the relation for the dissipation term in Equation 5 given by Equation 6:

$$\Phi = \varepsilon v_d g \Delta\rho \tag{6}$$

By integrating Equation 6 in Equation 5, and introducing the Peclet number by the relation $Nu = aPe^{-\frac{1}{2}} = a\left(\frac{v_d R_d}{K_{s,m}}\right)^{\frac{1}{2}}$, we can write:

$$\frac{dT}{dP} = \frac{3\rho_s c_{p,s}}{\rho_m c_{p,m}} \frac{T - T_{sm}}{R_d \rho_s g} aPe^{-\frac{1}{2}} + T \frac{\gamma}{K_{s,m}} + \varepsilon \frac{\Delta\rho}{\rho_s \rho_m c_{p,m}} \tag{7}$$

It is possible then to write a differential equation which has the form:

$$\frac{dT}{dP} + A(P)T = B(P) \tag{8}$$

where A and B are two functions given by main text Equations 15. The differential equation has a solution that yield Equation 2 used in the main text.

S2. Calculation of composition

First, we solve the chemical equilibrium in equation 8:

$$[(FeO)_x(NiO)_y(SiO_2)_z(Al_uCa_mMg_p)O + Fe_aNi_bO_cSi_d]$$

$$\updownarrow$$

$$[(FeO)_{x'}(NiO)_{y'}(SiO_2)_{z'}(Al_uCa_mMg_p)O + Fe_{a'}Ni_{b'}O_{c'}Si_{d'}] \tag{9}$$

$$\tag{10}$$

This reaction needs to satisfy the mass balance for each which is given by:

$$\begin{array}{lll} x+a & = & x'+a' \\ y+b & = & y'+b' \\ z+d & = & z'+d' \\ x+y+2z+u+m+p+c & = & x'+y'+2z'+u+m+p+c' \end{array} \tag{11}$$

where all the letter refer to a number of mole. The mass balance is completed by the exchange partitioning coefficient given by Equations 26. We get the following equations:

$$\begin{array}{lll} K_d^{Ni} & = & \frac{\chi^m_{Ni}}{\chi^{m.o.}_{NiO}} \frac{\chi^{m.o.}_{FeO}}{\chi^m_{Fe}} \\ K_d^{Co} & = & \frac{\chi^m_{Co}}{\chi^{m.o.}_{CoO}} \frac{\chi^{m.o.}_{FeO}}{\chi^m_{Fe}} \\ K_d^{Si} & = & \frac{\chi^m_{Si}}{\chi^{m.o.}_{SiO_2}} \left(\frac{\chi^{m.o.}_{FeO}}{\chi^m_{Fe}}\right)^2 \\ K_d^{V} & = & \frac{\chi^m_{V}}{\chi^{m.o.}_{V_2O_3}} \left(\frac{\chi^{m.o.}_{FeO}}{\chi^m_{Fe}}\right)^{3/2} \\ K_d^{Cr} & = & \frac{\chi^m_{Cr}}{\chi^{m.o.}_{Cr_2O_3}} \left(\frac{\chi^{m.o.}_{FeO}}{\chi^m_{Fe}}\right)^{3/2} \\ K_d^{O} & = & \frac{\chi^m_{Fe}\chi^m_{O}}{\chi^s_{Mw}} \end{array} \tag{12}$$

where χ^m_M and $\chi^m_{MO_{n/2}}$ are the molar fraction of metal and oxide of valence n, respectively. In the last equation of the system, the notation χ^s_{Mw} is referring to the amount of FeO in magnesiowüstite which is given by the formula of Frost et al. (2010) : $\chi^s_{Mw} = 1.148\chi^s_{FeO} +$

$1.319(\chi^s_{FeO})^2$.

Each K_d^M can be expressed as a function of the number of mole of the elements. As an example, we have for Ni, an element of valence 2:

$$K_d^{Ni} = \frac{b'}{a'+b'+c'+d'} \times \frac{x'+y'+z'+u+m+p}{y'} \times \left(\frac{x'}{x'+y'+z'+u+m+p} \times \frac{a'+b'+d'}{a'} \right)^{2/2} \tag{13}$$

For valence 2+ element, the sum of moles in each phases balances out, but not for 4+ (Si) or 3+ (V, Cr). In Equation 8, we purposely left out V, Cr and Co to simplify the calculation. These elements are solved later, which introduce a small error, but since their total abundances are low, the error in concentrations are low. All the initial conditions are known, the K_d^M are calculated from equation 25. The goal at each step is to find the value of x' (FeO) that will satisfied all the conditions, especially the value of K_d^O. Following the path detailed in the supplementary information of Rubie et al. (2011), expressing each number as a function of x' we get the system of equations: 14:

$$\begin{cases} a' &= a + x - x' \\ y' &= \frac{x'(y+b)}{a' K_d^{Ni} + x'} \\ b' &= y + b - y' \\ \alpha &= z + d \\ \gamma &= a' + b' + x + y + 3z + c - x' - y' + d \\ \sigma &= x' + y' + u + m + n \\ 0 &= [3x'^2 - a'^2 K_d^{Si}] z'^2 - [\gamma x'^2 + 3\alpha x'^2 + a'^2 \sigma K_d^{Si}] z' - \alpha\gamma x'^2 \\ c' &= x + y + 2z + c - x' - y' - 2z' \\ d' &= z + d - z' \\ \chi_{FeO} &= \frac{x'}{x'+y'+z'+u+m+n} \\ \chi^s_{Mw} &= 1.148\chi^s_{FeO} + 1.319(\chi^s_{FeO})^2 \\ K_d^{calc} &= \frac{a'c'}{\chi^s_{Mw}(a'+b'+c'+d')^2} \end{cases} \tag{14}$$

The value of x' is determined numerically to get $K_d^{calc} = K_d^O$, and the other molar abundances are then given.In the original paper, V and Cr were not included. Their valence in the conditions of planetary formation is 3+, therefore inserting V and Cr into equa-

tion 8 yields to non analytical solutions in the system 14. Therefore, once the system is solved without V and Cr, we use Equations 25 and 26 (Main text) to calculate the molar concentration of V and Cr. The mass balance is not respected, but given the low concentrations of both elements in either phase, the weight variation is less than 0.1 %. The number of mole for each phase are transformed back into mass by $m_i = \frac{n_i}{\mathbf{M_i}}$, where $\mathbf{M_i}$ is the molar mass of element (or oxide) i. Finally, we get the mass fraction in each phase by: $\chi_i^p(\%wt) = 100\frac{m_i}{m_p}$ where m_p is the mass of liquid metal or liquid silicate that equilibrated and m_i is the mass of the element i in the phase p. **S3. Discrimination of the results**

We tested 20 000 different values of the triplet (f_c, k, a_p). For every value we get a global composition for the mantle at the end of accretion using Equation 27 (Main text). We compare the concentration of each element to its concentration given in (McDonough & Sun, 1995), with the indicator $\delta^{BSE}\chi_i$ given by:

$$\delta^{BSE}\chi_i = \frac{|\chi_i^{model} - \chi_i^{BSE}|}{\chi_i^{BSE}} \tag{15}$$

where χ_i^{model} is the concentration (in mass fraction) of element i in the bulk mantle calculated by the model and χ_i^{BSE} is the concentration of element i in the BSE model taken as reference (McDonough & Sun, 1995). For each element, the number of solutions is not the same, as shown in Figure S3. As seen in this figure, some elements yields more solution than other. The minor elements (Ni, Co, Cr and V) and iron (Fe) are the elements for which the number of solutions is the lowest. Therefore, those are the elements that can discriminate the results. However, for a given value maximum error, the value of (f_c, k, a_p) which yields a solution for an element (for example Ni or Co) does not give a solution

for another element (Cr or V for instance). To simplify this problem, we use a weighted mean variation using the number of solutions presented in figure S3. The calculation is:

$$\delta^{\overline{BSE}}\chi = \Sigma_i \omega_i \delta^{BSE}\chi_i \tag{16}$$

where ω_i is the weight of each element normalized so that $\Sigma_i \omega_i = 1$. As shown in Figure S3, the number of solution for a givenn element is dependent on the maximum variation allowed, therefore ω_i values are not the same for the different maximum values. The values of ω_i are given in Table S3.

Using $\delta^{\overline{BSE}}\chi$ in Equation 16 we can get a larger number of solutions compatible with BSE composition than using $\delta^{BSE}\chi_i$, without having to chose an element. The number of solution depend on the maximum variation we allowed. In Figure S4, we can see that the solution space is increasing with the maximum value of $\delta^{\overline{BSE}}\chi$ retained. As can be seen in Figures S4 and S5, the discriminating factor for composition are a_P and f_c. Indeed, even for large values of $\delta^{\overline{BSE}}\chi$ (15 and 20 %), there is no solution for $a_P < 0.35$ or $f_c < 0.4$, while the entire value range of λ is spanned.However, for these values of $\delta^{\overline{BSE}}\chi$, a large number of concentrations are not representative of the BSE. For $\delta^{\overline{BSE}}\chi < 5\%$, the number of solution is quite low (n=22), and which means that no interesting inference can be made. Therefore, for the rest of the study, we use the condition $\delta^{\overline{BSE}}\chi < 10\%$, in agreement with the maximum error for most of the concentrations in the BSE model (McDonough & Sun, 1995) with a number of solution high enough (n=482) to interpret the effect of the different parameter.

When looking at the solution space for $\delta^{\overline{BSE}}\chi < 10\%$, it is possible to see that there is a limited range of values for a_P and f_c for which the output's mantle can be comparable to the BSE (Figure S5). For a_P the range is between 0.4 and 0.65, which means that the

final pressure of equilibrium is between 40% and 65 % of the final P_{CMB}, corresponding to final pressures at the bottom of the magma ocean $\simeq$ 55 GPa to $\simeq$ 80 GPa.

As for the f_c values, its range is between 0.6 and 1, with the higher number of solution for $f_c = 0.7$ (center panel of Figure S5). This means that at least 60% of the mass accreted should be reduced, and that it is possible to have 100 % of reduced accretion, but only for higher pressure of equilibrium. The values of a_P and f_c are compatible with the results of the original model of Fischer et al. (2015), which correspond to the case of $\lambda = 1$ for $f_c = 0.75$ and $a_P = 0.66$.

The value of λ does not have a strong effect on the composition, as can be seen by the flat distribution of solutions in Figure S5. This can be explained by the fact that the discriminating elements are Ni and Co: their concentration in the mantle is representative of the impactor composition and pressure at the end of accretion (see for instance the models of Wood et al., 2008; Bouhifd & Jephcoat, 2011; Fischer et al., 2015), for which the parameter λ has no effect by construction of the parameterized model (see Section 3).

S4. Heat transfer to the mantle

The last case we investigate is when $Pe \neq \infty$ and $\varepsilon = 0$. In this scenario, during the descent of each diapir toward the core, there is transfer of heat between metal and silicate. Equation 2 can be written:

$$T(P) = \left[\exp\left(-\int_{P_{eq}}^{P_{CMB}} \left(\frac{X(f)}{\rho_m(P')} - \frac{\gamma}{K_{s,m}(P')}\right) dP'\right)\right] \times$$

$$\left[T_{eq} + \int_{P_{eq}}^{P_{CMB}} \frac{X(f)T_{sm}}{\rho_m(P')} \exp\left(\int_{P_{eq}}^{P'} \left(\frac{\gamma}{K_{s,m}(P'') - \frac{X(f)}{\rho_m(P'')}}\right) dP''\right) dP'\right] \tag{17}$$

where T_{sm} is the temperature of the solid mantle, assumed to be equal to the solidus temperature given by Andrault et al. (2011):

$$T_{sm} = 2045\left(\frac{P_{eq}}{92} + 1\right)^{\frac{1}{1.3}}, \tag{18}$$

where P_{eq} is expressed in GPa. The function $X(f)$ is given by

$$X(f) = 3a\frac{c_{p,s}}{c_{p,m}}\frac{Pe^{-1/2}}{gR_d}, \tag{19}$$

where $a \approx 1$, $c_{p,s}$ and $c_{p,m}$ are constant heat capacity of silicate and metal respectively. The Péclet number is defined by equation 12; the diapir velocity is given by equation 7 with $\Delta\rho = \overline{\rho_m}(f) - \overline{\rho_s}(f)$. The error introduced in the value of Pe by using $\overline{\rho_m}(f)$ instead of the pressure-dependent density given by the EOS (equation 29) is on the order of 20%. The variation of temperature compared to a purely compressional heating case is dependent on the difference between the ratio $\frac{\gamma}{K_{s,m}}$ and $\frac{X}{\rho}$. The value of $K_{s,m}$ is in range of dozens of GPa, up to hundred of GPa and γ is between 1 and 2. The ratio $\frac{\gamma}{K_{s,m}}$ is therefore on the range of 10^{-11} to $10^{-9}Pa^{-1}$. The value of X depends on the value of Pe: the lower it is, the higher the value of X. Pe is dependent on R_d: the lower R_d is, the higher the value of Pe. g, R_d and Pe are constant for a given step of accretion, but their values evolve with the mass fraction accreted (see Table 1 in the main text). The radius of the diapir is assumed to be constant all along the accretion, and we tested values from 1 mm to 100 km. As shown in Figure S6, the effect of heat transfer are negligibles compared to the compression. The only effect seen is for $R_d = 1mm$ which is a highly improbable value in the core formation context. For $R_d > 10cm$, there is virtually no effect. Indeed, for $R_d = 10cm$, $Pe \sim 10^{-10}$, and the ratio X/ρ is close to $1GPa^{-1}$, which is at least one

order of magnitude less than the ratio $\frac{\gamma}{K_{s,m}}$ in the most favorable cases. This is why we neglect the heat transfer to the mantle in the main text.

References

Andrault, D., Bolfan-Casanova, N., Nigro, G. L., Bouhifd, M. A., Garbarino, G., & Mezouar, M. (2011). Solidus and liquidus profiles of chondritic mantle: Implication for melting of the Earth across its history. *Earth and planetary science letters*, *304*(1-2), 251–259.

Bouhifd, M., & Jephcoat, A. (2011, July). Convergence of Ni and Co metal–silicate partition coefficients in the deep magma-ocean and coupled silicon–oxygen solubility in iron melts at high pressures. *Earth and Planetary Science Letters*, *307*(3-4), 341–348.

Clesi, V., Monteux, J., Qaddah, B., Le Bars, M., Wacheul, J.-B., & Bouhifd, M. A. (2020). Dynamics of core-mantle separation: Influence of viscosity contrast and metal/silicate partition coefficients on the chemical equilibrium. *Physics of the Earth and Planetary Interiors*, *306*, 106547.

Fischer, R. A., Nakajima, Y., Campbell, A. J., Frost, D. J., Harries, D., Langenhorst, F., ... Rubie, D. C. (2015). High pressure metal–silicate partitioning of Ni, Co, V, Cr, Si, and O. *Geochimica et Cosmochimica Acta*, *167*, 177–194.

Frost, D. J., Asahara, Y., Rubie, D. C., Miyajima, N., Dubrovinsky, L. S., Holzapfel, C., ... Sakai, T. (2010). Partitioning of oxygen between the Earth's mantle and core. *Journal of Geophysical Research: Solid Earth*, *115*(B2).

Kuwayama, Y., Morard, G., Nakajima, Y., Hirose, K., Baron, A. Q., Kawaguchi, S. I., ... Ohishi, Y. (2020). Equation of state of liquid iron under extreme conditions.

Physical Review Letters, *124*(16), 165701.

McDonough, W., & Sun, S.-S. (1995). The composition of the Earth. *Chemical geology*, *120*(3-4), 223–253.

Rubie, D., Frost, D., Mann, U., Asahara, Y., Nimmo, F., Tsuno, K., ... Palme, H. (2011). Heterogeneous accretion, composition and core–mantle differentiation of the Earth. *Earth and Planetary Science Letters*, *301*(1-2), 31–42.

Wood, B., Wade, J., & Kilburn, M. (2008, March). Core formation and the oxidation state of the Earth: Additional constraints from Nb, V and Cr partitioning. *Geochimica et Cosmochimica Acta*, *72*(5), 1415–1426.

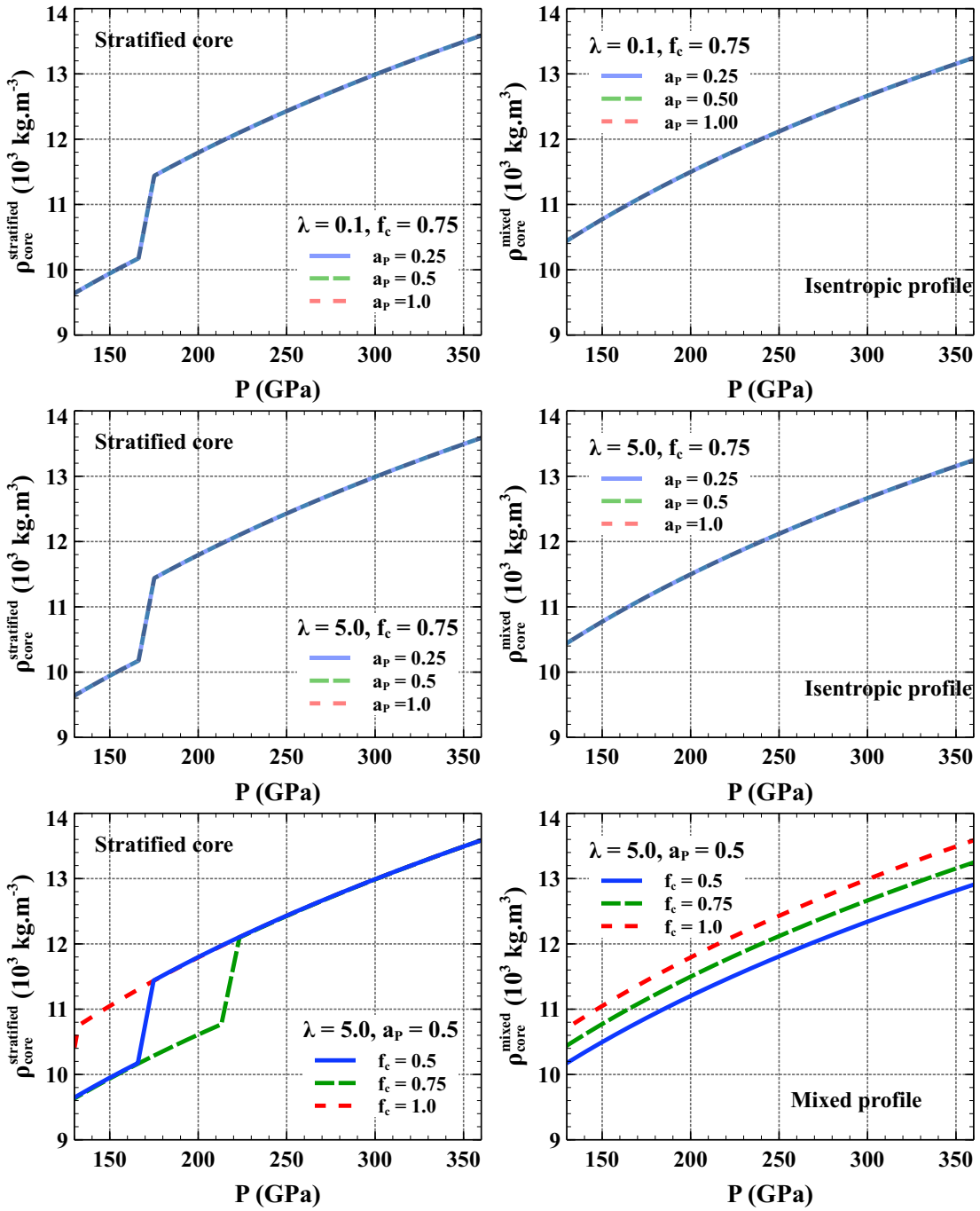

Figure S1. Density profile obtained before and after mixing for a simplified model presented in Section ?? of the main text. Each row correspond to the same conditions as in Figure ?? in the main text. The left column shows the stratified profile. The right column shows the mixed profile on which is calculated the isentropic temperature. Since it is a simplified model, the density changes only when parameter f_c is changed (last row). In the actual model, the compositionnal evolution is more complex.

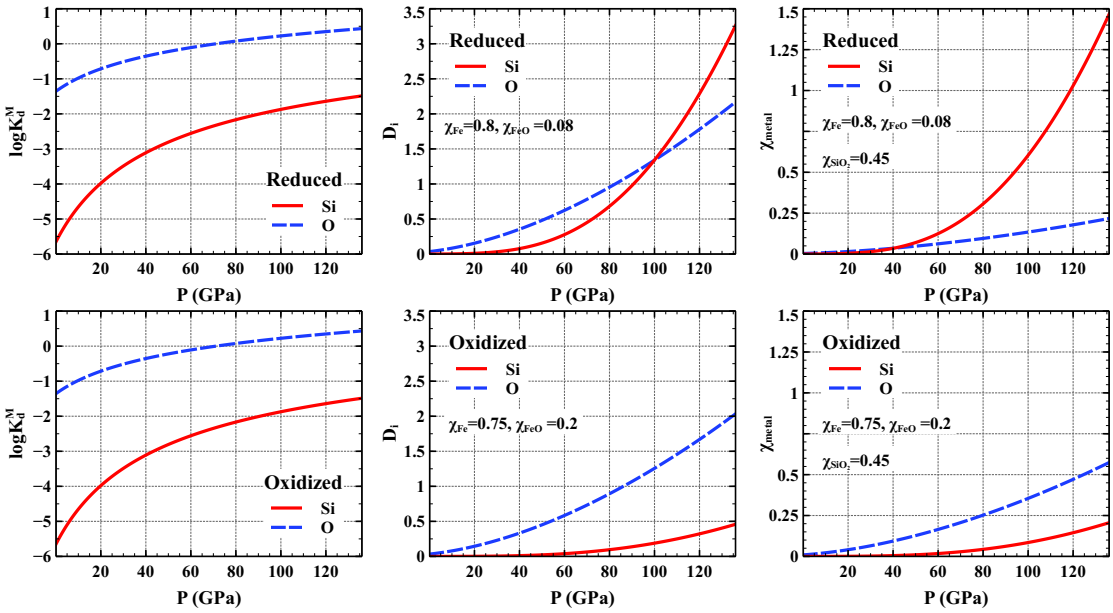

Figure S2. Illustration on a very simplified model on how oxygen is excluded from the core when the environment is reduced for the same P-T conditions. For each pressure of the x-axis here, the temperature is calculated using Equation 23. The left column are the results of calculation of $logK_d^M$ of Si and O (Equation 25)for the P-T conditions. The middle column shows a simplified estimation of the Nernst partitioning coefficient following Equation (15) of (Clesi et al., 2020). On the top row, it is calculated for a reduced environment with $\chi_{Fe} = 0.8$ and $\chi_{FeO} = 0.08$ (i.e. $logf_{O_2} \sim -2\Delta IW$). On the bottom row: oxidized environment with $\chi_{Fe} = 0.75$ and $\chi_{FeO} = 0.2$ (i.e. $logf_{O_2} \sim +1\Delta IW$). The third column give the resulting χ_{Si} and χ_O with the same $\chi_{SiO_2} = 0.45$ in both case. This figure shows that from the same values of K_d, it is possible to incorporate more

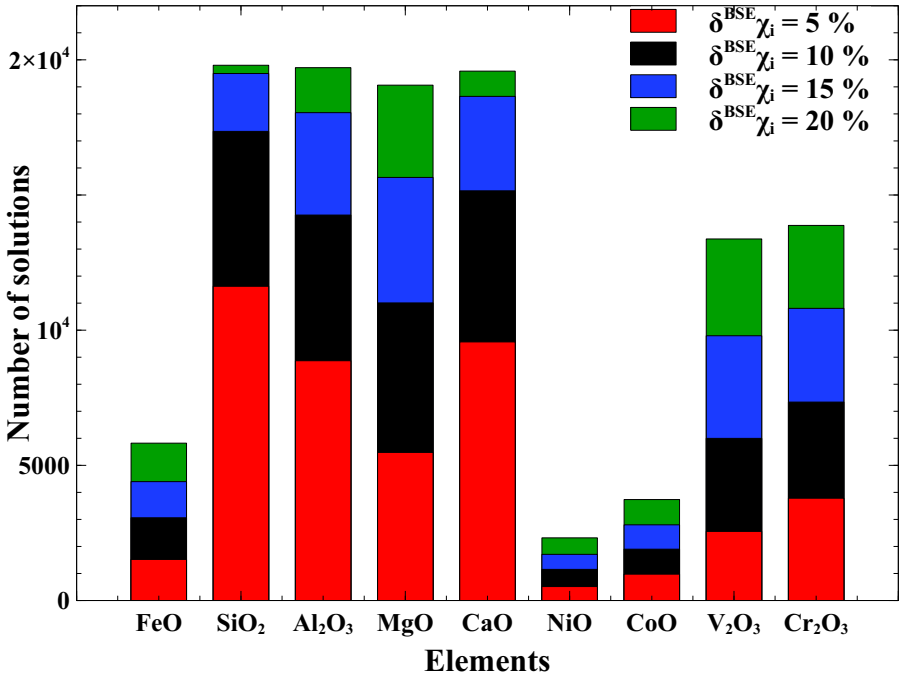

Figure S3. Number of solutions by element, for which the variation of concentration to the reference model ($\delta^{BSE}\chi_i$ calculated by Equation 15) is below 5% (red), 10% (black), 15% (blue) and 20 % (green). The maximum number possible is 20 000 (number of scenarios tested)

Element / Max Error	FeO	SiO_2	Al_2O_3	MgO	CaO	NiO	CoO	V_2O_3	Cr_2O_3
5%	0.138	0.018	0.024	0.038	0.022	0.407	0.215	0.082	0.056
10%	0.142	0.025	0.030	0.039	0.029	0.376	0.228	0.072	0.059
15 %	0.143	0.032	0.035	0.040	0.034	0.368	0.225	0.064	0.058
20 %	0.141	0.041	0.041	0.043	0.042	0.353	0.219	0.061	0.059

Table S1. Values of ω_i in equation 16 for different maximum variation. The weights are calculated by $\omega_i = (n_{min}/n_i)/Sigma_i(n_{min}/n_i)$ using the number of solution for element i n_i and the minimum number of solutions n_{min} in Figure S3. In all cases $n_{min} = n_{NiO}$.

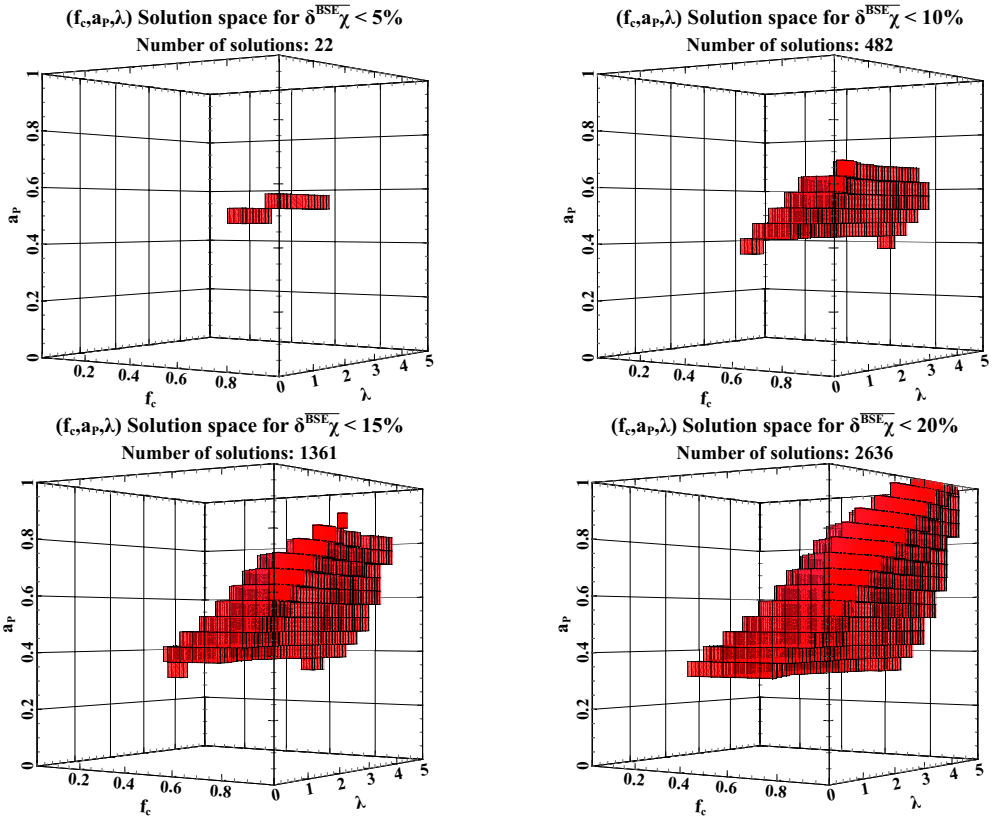

Figure S4. Solution space for $\delta^{\overline{BSE}}\chi$ inferior to 5%, 10%, 15% and 20%. The number of solutions increases as the mean variation gets higher.

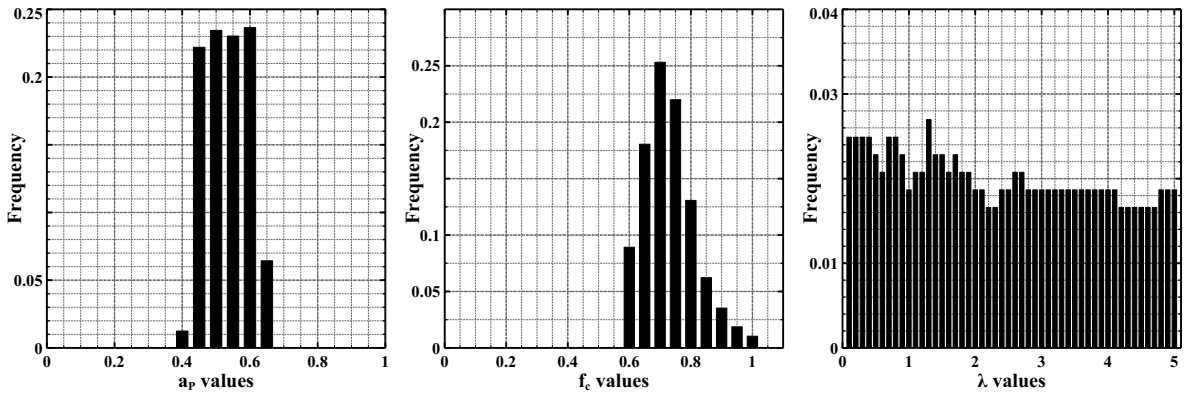

Figure S5. Frequency of solutions for a_P (left), f_c and λ (right) values for the condition $\delta^{\overline{BSE}}\chi < 10\%$. the total number of solutions is 482.

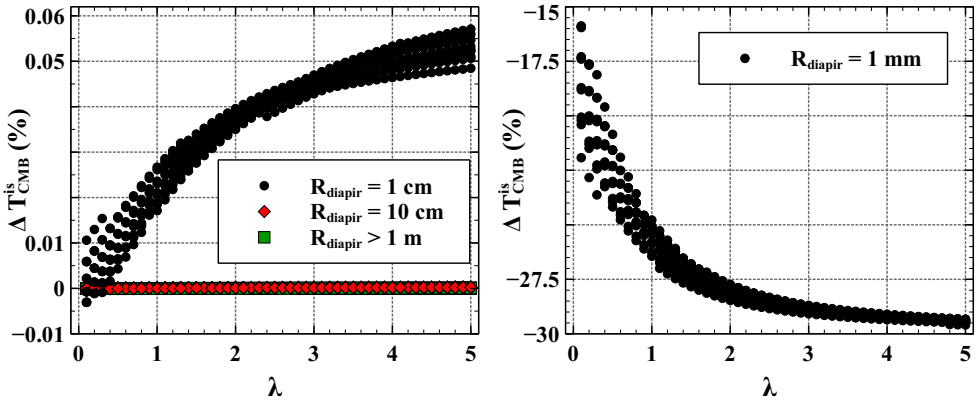

Figure S6. Relative variations of temperature when taking into account the heat transfers to the silicate compare to a case with purely compression (Equation 32). On the left are presented the case where $R_d > 1cm$ and on the right the case for $R_d = 1mm$.

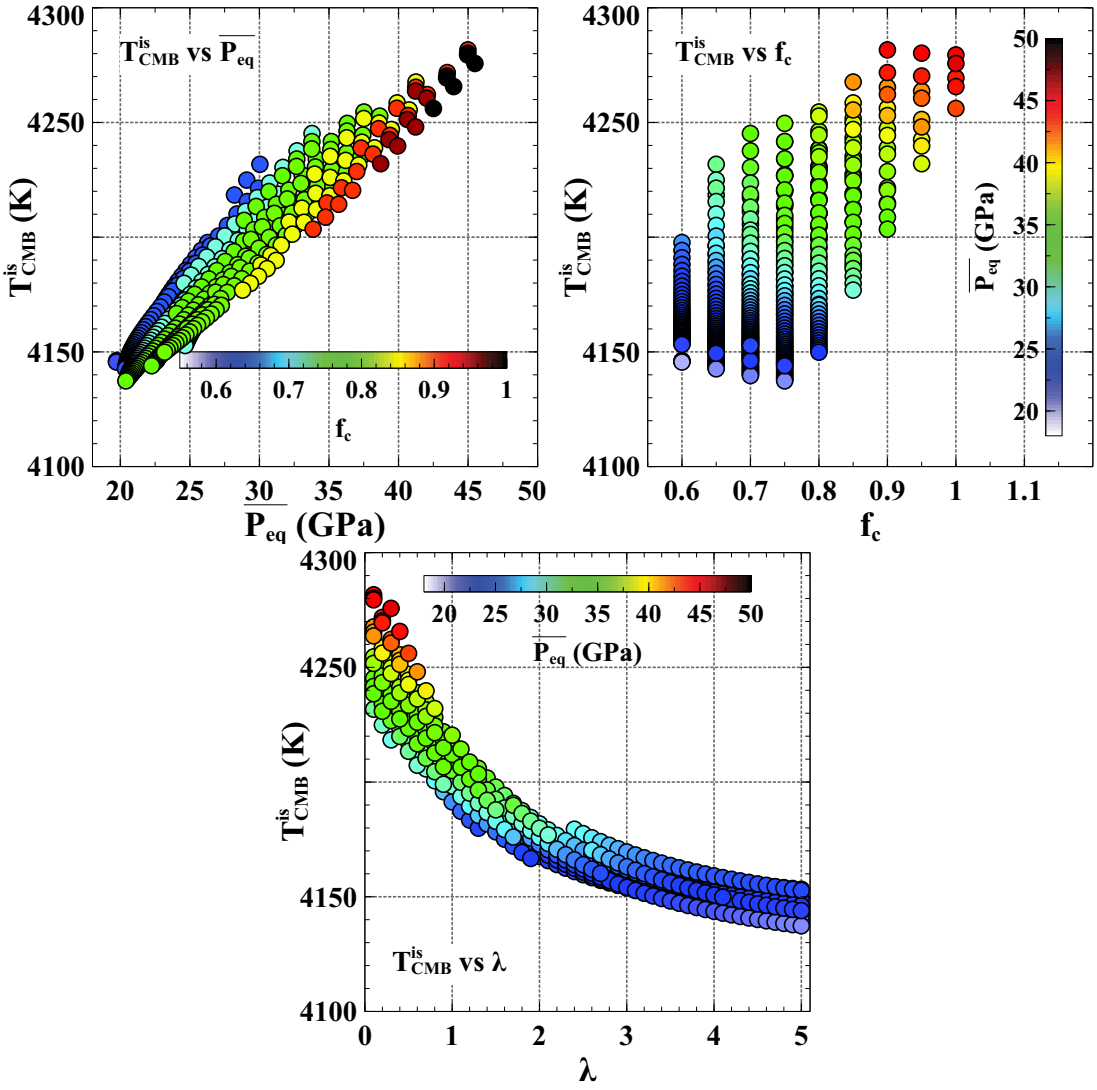

Figure S7. T^{is}_{CMB} vs $\overline{P_{eq}}$ (top left), f_c (top right) and λ (bottom), calculated with a gamma formalism from Kuwayama et al. (2020): $\gamma = \gamma_0 \left(\frac{\rho_0}{\rho_m}\right)^b$ with $\gamma_0 = 2.02$ and b = 0.63. The density profile is calculated from the same set of solutions as in the main text. With this formalism, the temperature are significantly different while still in comparable range.

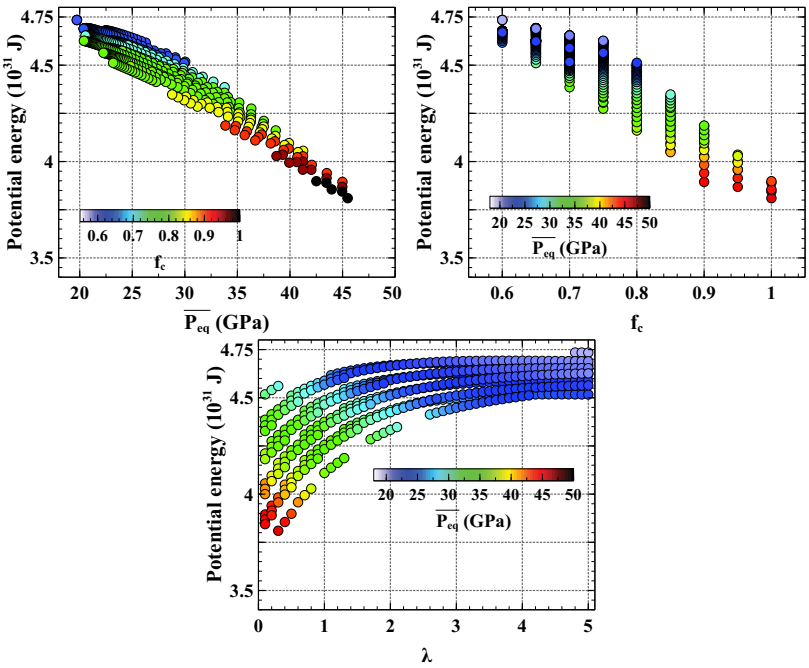

Figure S8. Potential energy of a stratified core calculated from Equation 38 as a function of $\overline{P_{eq}}$, f_c and λ.

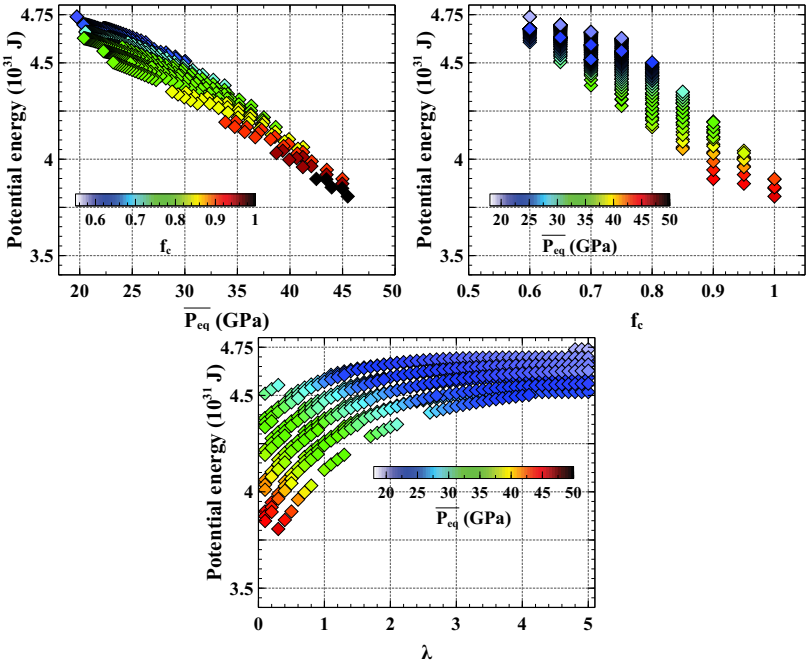

Figure S9. Potential energy of a mixed core calculated from Equation 38 as a function of $\overline{P_{eq}}$, f_c and λ.